

ISOLATED SAMPLING OF MUSCLES FROM
TANGENTIAL FLOW STREAM

By

Michael Dean Nofels

A DISSERTATION PRESENTED TO THE GRADUATE COUNCIL OF
THE UNIVERSITY OF FLORIDA
IN PARTIAL FULFILLMENT OF THE REQUIREMENTS FOR THE
DEGREE OF DOCTOR OF PHILOSOPHY

UNIVERSITY OF FLORIDA

2013

ACKNOWLEDGEMENTS

The completion of this dissertation would not have been possible without the encouragement, support and advice of Prof. and Mrs. ROBERTSON. Their contributions, suggestions, advice, criticism, and assistance in every phase of this work are largely responsible for this dissertation. I thank them both for their financial support during my graduate work.

I wish to thank Dr. John Landgren and Dr. Paul Ryan for the important part that they played in my education. I am especially appreciative of Dr. Landgren for his guidance, encouragement and confidence. He has provided me with opportunities for research, laboratory and field experience that were far beyond what is expected of a graduate student.

I wish also to thank Mrs. Emily Skerfving for her assistance in preparing this manuscript.

Finally, I wish to thank my parents for their advice and encouragement, and my wife Ellen for helping me through the difficult times.

TABLE OF CONTENTS

	Page
ACKNOWLEDGMENTS	ii
LIST OF TABLES	iv
LIST OF FIGURES	viii
LIST OF SYMBOLS	xi
PREFACE	xiii
CHAPTER	
I INTRODUCTION AND NECESSARY AUXILIARY THEORY	1
a. Introduction	1
b. Instrumental Sampling Theory	1
II REVIEW OF THE RELEVANT LITERATURE	26
A. Summary of the Literature on Asynchronous Sampling	26
1. Sampling from Run to Unordered Subintervals	26
2. Sampling from Run to Basic Subintervals	27
B. Summary of the Literature on Synchronous Plans	31
1. Codes and Characteristics of Synchronous Plans	31
2. Errors Induced by Synchronous Plans	31
3. Errors due to the B Type Power Take	35
4. Methods Available for Measuring Relative Components in a Synchronous Plan Portal	37
5. BSA Criteria for Sampling Synchronous Plans	44
III EXPERIMENTAL APPARATUS AND METHODS	48
A. Experimental Design	48
B. General Description	51
1. Sampling Plan Generator	51
2. Program Policy	52
C. Timing Considerations	54
D. Selection of Sampling Intervals	57
E. Sampling Results	57

CHAPTER	Page
I Analytical Procedures	14
1 Air Velocity Profiles	14
2 Air Pressure Profiles	14
3 Sampling Procedures	14
4 Trajectory Flow Mapping	14
II RESULTS AND ANALYSIS	14
A Analytical Sampling Experiments	14
1 Station Number	14
2 Sampling with Parallel Flow	14
3 Analysis of Probe Data	14
4 The Effect of Angle Misalignment on Sampling Efficiency	14
5 The Effect of Angle Misalignment and Unidirectional Sampling Velocity	14
B Trajectory Flow Mapping	14
F EVALUATION OF AN IPI METHOD: A METHOD THAT IS A TRAJECTORY FLOW METHOD	117
III SUMMARY AND DISCUSSIONS	111
A Summary	111
B Recommendations	114
REFERENCES	114
ACKNOWLEDGMENT	114

Table of Contents

Title	Page
I FLOW FIELD STUDIES AT VARIOUS WINDMILL LOCATIONS	11
II CHARACTERIZATION OF A POINT FOR DIFFERENT SAMPLING ANGLES	24
III DISCUSS THE RESULTS	26
IV MEASUREMENTS OF EXPERIMENTAL AIRFLOW	32
V TABLE OF MEASUREMENTS WINDMILL IN 10 m DUCT	34
VI TYPICAL VELOCITY PROFILES IN THE EXPERIMENTAL AIRFLOW SYSTEM	36
VII MEASUREMENTS OF SAMPLING WITH TWO PARALLEL WINDMILLS	47
VIII MEASUREMENT OF PARTICULATE MATTER COLLECTED IN THE FRONT WIND FOR VARIOUS WINDMILLS WITH THE FLOW STRAIN	54
IX MEASUREMENT OF PARTICULATE MATTER COLLECTED IN THE FRONT WIND FOR WINDMILLS OF AN AREA OF 40 SQUARE METERS WITH THE FLOW STRAIN	56
X ADAPTATION COEFFICIENT AS A FUNCTION OF STRAIN RATIO FOR 10 SQUARE METERS	75
XI ADAPTATION COEFFICIENT AS A FUNCTION OF STRAIN RATIO FOR 40 SQUARE METERS	77
XII ADAPTATION COEFFICIENT AS A FUNCTION OF STRAIN RATIO FOR 10 SQUARE METERS	82
XIII COMPARISON OF SAMPLING EFFICIENCY RESULTS WITH THEORY OF BURNETT AND SPILLER FOR $B = 0.1$, $B = 0.2$ AND $B = 0.3$	83
XIV ADAPTATION COEFFICIENT AS A FUNCTION OF STRAIN RATIO FOR $B = 0.1$, $B = 0.2$ AND $B = 0.3$	84

LIST OF TABLES (continued)

Table		Page
VI	ADHESION COEFFICIENT AS A FUNCTION OF SPREAD VOLUME FOR $\theta = 0$ & $\theta_c = 90^\circ$	91
VII	ADHESION COEFFICIENT AS A FUNCTION OF SPREAD VOLUME FOR $\theta = 45^\circ$, $\theta_c = 2.5$ AND 5.0	91
VIII	ADHESION COEFFICIENT AS A FUNCTION OF SPREAD VOLUME FOR $\theta = 0$ & $\theta_c = 90^\circ$	91
VIII	ADHESION COEFFICIENT AS A FUNCTION OF SPREAD VOLUME FOR $\theta = 0$ & $\theta_c = 90^\circ$	91
IX	LOCATION OF SUPPLY POINTS.....	92
X	FEASIBLE FIRST FIVE MEASUREMENTS MADE AT 1 SPATTER CONDITION OF THE DISK.....	95
XI	FEASIBLE FIRST FIVE MEASUREMENTS MADE AT 2 SPATTER CONDITION OF THE DISK.....	99
XII	FEASIBLE FIRST FIVE MEASUREMENTS MADE AT 4 SPATTER CONDITION OF THE DISK.....	99
XIII	FEASIBLE FIRST FIVE MEASUREMENTS MADE AT 8 SPATTER CONDITION OF THE DISK.....	99
XIV	FEASIBLE FIRST FIVE MEASUREMENTS MADE AT 16 SPATTER CONDITION OF THE DISK.....	100
XV	APPROX CHAIN SECTORIAL VOLUME AS A FUNCTION OF DISK POSITION AND FLUX DENSITY.....	102
XVI	5-TYPE FIRST FIVE MEASUREMENTS MADE AT THE 5.0 SUPPLY POINT FOR THE 16 FLUX CONDITION.....	103
XVII	5-TYPE FIRST FIVE MEASUREMENTS MADE AT THE 8 SUPPLY POINT FOR THE 16 FLUX CONDITION.....	103
XVIII	MEASUREMENT PARTICLE DIAMETERS FOR THE 10 PERCENT INTERVAL OF THE SIZE DISTRIBUTION FOR $\theta = 0$ & $\theta_c = 2.5$	104

LIST OF TABLES—continued

<u>Table</u>		<u>Page</u>
IX.11	REFLECTION COEFFICIENT CALCULATED IN THE TEMPERATURE MODEL FOR THE LOW FLOW CONDITION	104
IX.12	REFLECTION COEFFICIENT CALCULATED IN THE TEMPERATURE MODEL FOR THE HIGH FLOW CONDITION	105
IX.13	RESULTS OF THE GEOMETRIC SURFACE SIMULATION MODEL FOR TEMPERATURE CONDITIONS	107
IX.14	SUMMARY OF EQUATIONS PROVIDING FURTHER TABLES FOR	109

LIST OF SYMBOLS

Page	Page
1	1
2	2
3	3
4	4
5	5
6	6
7	7
8	8
9	9
10	10
11	11
12	12
13	13
14	14
15	15
16	16
17	17
18	18
19	19
20	20
21	21
22	22
23	23
24	24
25	25
26	26
27	27
28	28
29	29
30	30
31	31
32	32
33	33
34	34
35	35
36	36
37	37
38	38
39	39
40	40

LIST OF FIGURES

Figure	Page
15a	General view of a dovetail plate tube
15b	Front view of a dovetail plate tube
16	Flow hole plate tube assembly as per fig 14
17	Front view of plate tube assembly as per fig 14
18	Experimental set up
19	Sampling system
20	Typical velocity profile in experimental test section
21a	Experimental system for measuring cross sectional flow profiles in a swirling flow section
21b	Control used in the study to generate swirling flow
22	Photograph of the 3-dimensional plate with top reversing valve. Shows the location of the pressure taps
23	Sampling efficiency vs. Stokes number at 30° misalignment for $U = 1$
24	Sampling efficiency vs. Stokes number at 30° misalignment for $U = 2$
25	Sampling efficiency vs. Stokes number at 30° misalignment for $U = 1$
26	Stokes number at which 1% collection error occurs vs. misalignment angle
27	U^* vs. adjusted Stokes number for 30, 45 and 60 degrees
28	Deposition coefficient vs. Stokes number. Model prediction and experimental data for 30, 45 and 60 degrees
29	Predicted capture coefficient vs. Stokes number for 30, 45, 60, 75 and 90 degrees

LIST OF FIGURES—continued

Figure	Page
33 Comparison of experimental data with results from Refs. 1 and 2 (a)	81
34 Sampling efficiency vs. Stokes number at 40° misalignment for $S = 1.0$ and 2.0	82
35 Sampling efficiency vs. Stokes number at 40° misalignment for $S = 2.0$ and $S = 3.0$	83
36 Sampling efficiency vs. Stokes number at 30° misalignment for $S = 1.0$	100
37 Cross-sectional view of a tangential-flow stream leaving plane rotors (dimensions, sampling process, and the negative pressure region)	102
38 Detail of the negative region R and the zero area along the side of the duct	110
39 Detail of the tangential velocity component along the side of the duct	111
40 Location of the negative pressure region as a function of duct-to-disk dimension from the tip of	114
41 Particle size distribution used in the computer model	120

SYMBOLS

- R = radius of sampler inlet
- R_p = projected area of sampler inlet
- U_a = area of orifice tube approaching nozzle
- U = ratio of measured concentration to true concentration
- V = sampling orifice tube diameter
- V_a = flow concentration in inlet
- V_s = flow concentration in flow stream
- V_r = concentration ratio of forced gas sampling solution
- V_p = sampling flow rate
- V_i = inlet diameter
- V_p = orifice diameter
- u = measured injection pressure
- u = adjusted static pressure
- l = sampling distance
- l = withdrawal distance upstream from nozzle
- n = constant
- P = ratio of free stream velocity to inlet velocity
- C = constant
- V_x = axial component of stack velocity
- V_y = velocity in inlet
- V_z = radial component of stack velocity
- V_{xy} = free stream velocity

- (α) : porosity, (depends of compaction)
- (\bar{p} , \bar{p}') : Functions increasing absolute pressure with distance from left to right
- (ρ_0) : particle density
- (θ) : viscosity
- (α) : angle of the flow stress with respect to the crack axis
- (α) : angle of alignment of nuclei with respect to the flow stress
- (τ) : particle relaxation time
- (Δp) : pressure difference

Division of Historical Geography, The Senate Chamber
of the University of Toronto, 177-181 PAVILLION of the
University for the Faculty of Arts, University of Toronto

MANUSCRIPT RECEIVED 10 JANUARY 1988

10

Figure 6

[illegible][illegible]

Region	Country	Year	Population	Urban population	Population density	Urban population density
North America	USA	2000	281,421,906	194,489,000	30.1	10.7
Europe	Germany	2000	82,164,700	50,000,000	231.1	10.7
Asia	China	2000	1,210,262,000	393,000,000	151.1	10.7
South America	Brazil	2000	158,417,700	100,000,000	16.6	10.7
Africa	Nigeria	2000	119,399,000	50,000,000	151.1	10.7
Oceania	Australia	2000	20,063,600	10,000,000	3.2	10.7

A comprehensive analysis of sampling errors is carried out in this paper, which is a thorough study of sampling the particles in a fluid jet. Among the aims of a system is to determine the errors involved in sampling particulate matter from a turbulent flow stream. Two methods are compared, one instantaneous and the other instantaneous, were taken from a jet of fluid sampled and compared to dynamic sampling. This is a function of Stokes Number. Interdispersed aerosol particles 1 to 11 μ m in diameter, generated with a rotating disc aerosol generator, and suitably dispersed in air at different points were used as experimental aerosols. The dust collector was varied from 100 to 400 cm/min and the nozzle diameter of 2.445 and 2.54 cm were used to obtain values of Stokes number from 0.001 to 0.01. Experiments were performed at flow angles of 10, 45 and 90 degrees to determine the errors associated with sampling with an instantaneous sampling velocity and with the nozzle sampled with the flow stream. The sampling test represented a dimensionless fluid of 11 μ m of a value of Stokes number between

1 and 2 depending on the desired measurement. The two common cases are alignment, angle versus the perpendicular (proper), and the angle of force the body exerts a perpendicular as a function of angle was developed to adjust the data when in contact for this.

Using an equation experimentally developed from three point contact and using the equation of balance and force resulting from contact coupling this with two intelligent, a differential ratio was developed and tested which predicts the coupling force when both mass displacement and contact force coupling variables were simultaneously. It was found that the coupling that approached a constant force (1-gram) above 8 is the ratio of the force versus velocity to the coupling velocity. During the testing, it was discovered that as much as 60% of the pendulum mass entering the swing occurred in the middle and front half of the three bodies. Impulse times of this phenomenon were noted for possible coupling and analysis are discussed.

The masses and characteristics of suspended film systems are described as they relate to systems in contact coupling. The definition of the 3 point film tube was used as a starting point for discussion. A three dimensional or three body point tube was used to test three horizontal and vertical film patterns in a stack following the action of a critical. Angles as great as 70 degrees relative to the axis of the stack and a critical film were also used in the study.

Using information found in this study a correlation model was developed to determine the forces involved when making a limited 3 matrix to a two point film system. For an overall work a 10 to 100 (mass ratio) distance

and geometric standard deviation (σ_g) of $10^{+1.2}$. The predicted concentrations are 50% less than the true concentration. For an actual dose of 10 mg/kg and σ_g of 2.0, a 50% error was produced. Flow rates determined by the II type plate were from 50 to 50% greater than the actual flow rate. Explanations of these results are described and recommendations for installation of the United States supply train for use in a suspended flow stream are described.

CHAPTER I
INTRODUCTION AND STATEMENT OF THE PROBLEM

A. INTRODUCTION

This study deals with the problem of obtaining a representative sample of particles within flow systems where flow conditions prevail in the units of the study, as in the case of manufacturing liquid flow. This type of flow is commonly found in units which could be the source of substantial sampling errors. The causes and characteristics of this particular flow pattern are described and the errors encountered in particulate concentration and moisture wet determinations are thoroughly analyzed and discussed.

The analysis of sampling errors is approached from two directions in this study. One approach involves an investigation of normal sampling bias due to nonrandom sampling techniques and misalignment of the units with respect to the flow stream as a function of particle and flow characteristics. The second part of the study involves an accurate analysis of the flow patterns in a turbulent flow system. The information obtained in the two parts of the study will be combined to evaluate the errors that could be encountered when relying on the normal \bar{X} (s, \bar{S}) analysis in a turbulent flow system.

Consider an representative sample of particles entering a unitary cross section, σ , in a beam of sample incident velocity v . The unitary cross section is defined by the condition: (2) (3) The current of incoming particles, Φ_0 , must be equal to the flux across velocity v and to the total flux in a region parallel to the flow direction. If these conditions are normalized the frontal area of the sample, A_0 , will be equal to the area of the cross section of the flow stream entering the unit. Denote A_0 (see Figure 1). Then, there will be no divergence of trajectories either any form or area the particle and the particle distribution on the inlet, ϕ_0 , will be equal to the particle distribution on the flow stream, ϕ .

The dynamics of streamlines is governed by supermolecular
 coupling. Independent coupling or decoupling, there is a
 possibility of particle size fractionation due to the inertial
 properties of particles. In the case of supermolecular coupling,
 (see Figure 2) the coupling velocity, V_c , is greater than the flow
 stream velocity V_s . Therefore, the rate of the flow stream that is
 coupled v_c will be greater than the decoupled arm of the coupling
 velocity v_d . All of the particles that are in the projected area A_p ¹
 will enter into the wells. Particles outside this area but within A_p
 will have to wait until the streamlines in order to be collected. In
 some of their history, some of the target particles will be unable to
 enter the zone and will not enter the coupling wells. Since not all of
 the particles in the coupled area A_p will be collected, the measured
 concentration will be less than the actual concentration.

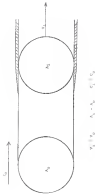


Figure 1. Nonlinear coupling.

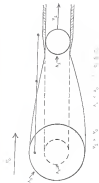


Figure 3 Superconducting coupling

Subsidiary coupling defines the condition in which the coupling velocity is less than the flow stream velocity (see Figure 3). In this situation the frontal area of the nuclei, A_N^1 , is greater than the projected area of the flow, A_F . The volume of air lying within the projected area, A_F , but outside A_N will not be sampled and the measurement will depend upon the nuclei. However, some of the particles in this area, because of their motion, will be unable to negotiate the turn with the streamlines and will be collected in the nuclei. However, none of the particles within the sampled area A_N will be influenced along with all of the particles within A_F , the measured concentration will be greater than the actual particle concentration.

The bias due to misalignment of the nuclei with the flow stream is similar to that caused by supersidiary coupling. When the nuclei is at an angle to the flow stream (Figure 4) the projected area of the nuclei is reduced by a factor equal to the cosine of the angle. Again, if the nuclei velocity is equal to the flow stream velocity, a reduced concentration will be obtained because none of the larger particles will be unable to negotiate the turn with the streamlines. Therefore, whenever the nuclei is misaligned the concentration measured will always be less than or equal to the actual concentration.

For all three conditions of subsidiary coupling (supersidiary, subsidiary, and nuclei misalignment), the magnitude of the measured concentration error will depend upon the size of the particles. More specifically it will depend upon particle inertia, which implies that the velocity and density of the particles are also important. Particle

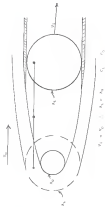


Figure 1. A hand-drawn diagram of a mechanical system.

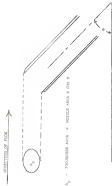


Figure 4. The effect of nozzle misalignment with flow stream.

energy projection function to the two KCH 14 magnetic fields, the (3) detector will advantage the concept of zero. Therefore, in all cases, active sampling arrays will accept the target particles and higher velocities.

Before discussing the direction of the sampling bias, it is also possible to predict theoretically the statistic and measure error for a given resolution. This can be done by considering what happens when the location of the particles is very small ($l \ll \lambda$), the particles can negotiate any turn that the streamlines make and what happens when the location of particles is very large ($l \gg \lambda$) the particles are unable to negotiate any turn with the streamlines. In the former case of very low location, it can easily be seen that since the particles are very small they do not leave their streamlines and therefore there will be no sampling bias. In this situation the concentration of particles cannot be statistically altered regardless of sampling velocity or whether the nozzle is aligned with the flow stream. Thus, first, a velocity error of 1 is obtained for small location particles.

The velocity error that can theoretically occur in statistical sampling depends on both the velocity ratio R where

$$R = V_s/V_d \quad (1)$$

and the alignment angle θ .

In the case of streamlines for very high particle particles which are unable to negotiate the change of direction, only those particles directly in front of the projected nose of the nozzle ($\theta = 0$) will enter the nozzle regardless of the sampling velocity. Therefore,

the concentration collected by the aerosol collector being the number of particles meeting the nozzle, $A_1 V_1 C_{p1}$, divided by the volume of air sampled, $A_2 V_2$.

$$C_1 = \frac{A_1 V_1 C_{p1}}{A_2 V_2} = \frac{C_{p1} A_1}{A_2} \quad (2)$$

The ratio of the sampled concentration to the true concentration then is equal to the inverse of the velocity ratio. Therefore, the maximum sampling error for the condition of unaided interception is equal to V_2/V_1 or 0. For example, if the sampling velocity is twice the free stream velocity, the resulting concentration will be only half the actual concentration.

For the case of a cylindrical nozzle, a similar analysis is applied for the particles with very large inertia, only those flying directly in line with the projected frontal area of the nozzle will be collected. The measured concentration could again be the number of particles intercepted at the nozzle, $A_1 \text{ sec} V_1 C_{p1}$, divided by the volume of air sampled, $A_2 V_2$. Therefore, the ratio of the measured to the true concentration would be $V_2 \text{ sec} A_1/V_1$ or 0.5:1. This represents the maximum sampling error for unaided interception.

CHAPTER 11
EFFECTS OF THE PARTICULATE CHARACTERISTICS

1. Summary of the Literature on Particulate Deposition

1.1. Depositing Gas Due to Gravitational Settling

Research activities have been active, describing the sources and statistics of various atmospheric conditions and the mechanisms of deposition of the various gases. Lapple and Shepherd (2) studied the deposition of particles in a flow system and presented a formula for calculating the value of the magnitude of various resulting rates. There is a difference between the average sampling velocity and the local flow station velocity. Brown (3) examined errors in the value of local sampling of spherical particles of 1 and 11 microns mean diameter (400) and found the relationships shown in Figure 1. Super diffusible sampling (sampling with initial velocity greater than the free stream velocity) leads to a concentration lower than the actual concentration, while subdiffusive sampling has the opposite effect. Brown found that the magnitude of the error was not only a function of particle size in microns in Figure 1, but also of the velocity and the particle diameter. He proposed that the sampling efficiency was a function of the dimensionless particle inertial parameter I . (Higher number) defined as:

$$I = \frac{C_p \rho_p d_p^2 V_{rel}^2}{18 \mu_g^2} = \frac{V_p^2}{V_g^2} \quad (1)$$

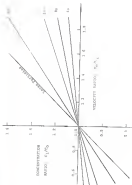


Figure 1 Relationship between the mass fraction of volatile matter and the volatile matter ratio for various fuels (from Table 1)

where

$$L_p = \text{sample length (meters)}$$

$$L = \text{Laminar penetration length (meters)}$$

$$A_p = \text{particle area (m}^2\text{)}$$

$$\tau = \frac{A_p \rho_p}{\rho_g} \text{ (sec)}$$

$$A_g = \text{cross-section of jet}$$

$$D_j = \text{jet diameter}$$

The relationship that is defined by (1) is generally not unique to estimate the degree of dilution. Brown and Smith (1971) gave a relationship between velocity and L_p . The velocity was 0.75 m/s; the velocity L_p was 0.001 for the 50 micron particles and between 0.5 and 1.0 for the 4 micron particles.

More recently, Smith et al. (1974) on a suspension of carbon precipitated fly ash 14 μ m MVD, showed only a 10% negative error in calculated concentration for sampling velocities 40% greater than the Stokes. There was an atmospheric flow of 0.1 μ m MVD produced at downstream concentrations changes were while sampling at a 40% variation from ambient flow. This indicates that estimates sampling is relatively insensitive for fine particles. Brown and Smith (7) extended their use to the relationship coupling of particles in three size ranges 10-12, 25-100, and 400-800 μ m and in a range of nuclei to mass velocities of 0.5 to 1.0. They found that above the velocity nuclei 0 range from 0.5 to 1.0 the coarse particles were not by substantially 50%, and that sufficient nuclei velocities resulted in greater errors than Stokesian nuclei velocities. In addition, they found that for the entire particles, the velocity into the nuclei had an important

leading to the quantity of dust collected. They suggested using the product of the mean area and the mean gas velocity approaching the nozzle as the gas sample volume, independent of the velocity of the nozzle. By using their method for particles greater than 10 μm , it is possible to obtain small deviations even when deviations from stochastic velocity are quite large. Whitby and Lind (3) also observed that calculating the dust concentration from the approach velocity (instead of the actual sampling rate) produced only slight errors when sampling $\text{H}_2\text{SO}_4/\text{H}_2\text{O}$ for large particles.

Katafuchi and Nakano (3) found the sampling bias or efficiency coefficient, E , to be a function of the aerodynamic parameter K and the velocity ratio R . They developed a chart which can be used to predict values associated with sampling bias depending on both K and R . Nakano et al. (4) experimentally defined the dependence of the efficiency upon particle inertia and the velocity ratio. In a slightly different nomenclature:

$$E = V_p/V_a = 1 + (3-1) \cdot R(K) \quad (3)$$

where $R(K)$ is a function of inertia given by

$$R(K) = [1 - \exp(-K^2/2)]/K^2 \quad (4)$$

K is the stopping distance or the distance a particle with initial velocity V_p will travel into a still fluid before coming to rest and is defined by (11):

$$K = V_p^2/g \quad (5)$$

is $U = 4\pi n_0 \lambda^2 \sin^2 \theta / 2$ (where n_0 is the number of the Fe^{2+} ions located by the detector in unit cm^2), λ is a function of the particle diameter and is given by the equation

$$\lambda = \pi D^2 / 4 \quad (10)$$

It was shown that U has a maximum at $\theta = 45^\circ$ and $U = 0.5$ (10).

Flash illumination photographic techniques were used by Fujiwara and Kishi (12) to study particle ejection. Photographic observations enabled them to verify Ishiguchi's claim that 1. the undisturbed flatness spectrum of the particle was between 3 to 4 times the diameter of the particle. They examined the data of previous studies on error due to diffractional spreading and concluded that the discrepancy between experimental data was due to the researchers failing to take into account three things: 1) particle ejection on the inner channel of the sampling device, 2) rebound of particles from the front edge of the sampling nozzle and their subsequent reposition into the nozzle, and 3) the shape and size distribution of the nozzle. They also found that the sampling efficiency was a function of the inner diameter of the nozzle, D_i , as well as L and R .

In a more recent article, Ishigawa and Kishi (13) examined the dependence of the function $U(Q)$, in equation (1), on both the particle separation parameter, L , and the velocity ratio, R . Previous authors (12, 14) had concluded that $U(Q)$ was a function of L alone, but Fujiwara and Kishi obtained experimental data demonstrating that for thin-walled nozzles, $U(Q)$ was also a function of R . Equations were developed from the data for values of L between 0.15 and 4.0 and for values of R between

$$B(\mathbf{R}, R) = 1 - 1/(1 + R^2) \quad (13)$$

where

$$R = 2 + 2 \sin^2(\theta/2) \quad (14)$$

Figure 1 shows a plot of equations (12)–(14) for a range of initialy values and helicity numbers. The most significant changes in the capture cross-section occur at values of k between 0 and 1. Around $k = 1$, the capture cross-section tends to asymptotically approach its theoretical limit of R_0 . Beyond a helicity number of about 4, it can be assumed that the capture cross-section equals R_0 . This can be predicted both from equations (12)–(14) and from theoretical considerations. Bellack (10) and Bellack and Levin (11) have shown that the capture cross-section is always at approximately a constant fraction of the radius. Therefore, a particle interacting at a velocity V_{rel} will have to change direction by an amount of the order of (R_0/V_{rel}) . If a particle could change direction by that amount of time it will not be able to make the turn with the circulation. Since τ represents the amount of time required for a particle to change direction, setting $\tau = (R_0/V_{rel})$ represents the limiting time particle will still be able to make a turn with the circulation. Rearranging shows that it can be seen that this situation occurs when $V_{rel}/R_0 = \pi$ or at a helicity number of 4.

Section 3.1.1 further analysed the capture cross-sections from purely radial as well as particle diameter when sampling systems for

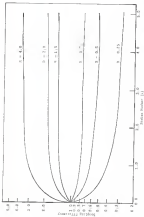


Figure 4. Coupling efficiency as a function of fiber radius r for various values of n .

analyzing consequences cannot obtained when sampling schedule provided, 0.1 to 0.40 and 1.20 percentage standard deviations, sampling at near ends and separate velocities. He obtained sample variances which were greater than the true variances when the sampling velocity was 30% of the true signal velocity (20%).

Richard [14] studied the instantaneous sampling of nonstationary processes in a 1-D link system and found that it is possible to sample a 10% nonstationary input signal sampling independently with a small number of samples. Richard also showed that for all nonstationary sampling velocities, the nonstationary series were not significantly related with discrete random.

5. Sampling Error Due to Axial Misalignment

Sampling error associated with the axial misalignment has not been adequately evaluated in past studies because the sampled data field was not used or cannot control its velocity and position in the data sets. The studies that have been performed on the effect of point misalignment do not provide enough quantitative information to understand why this part the basic causes of the problem. Studies were provided through investigations by Richard and Langford, as reported by White [1] on the effect of misalignment on the collection efficiency of 4, 11 and 17 in particular (see Figure 7). In a study by Osherson [17] on the directional dependence of the sampled, it was found that a sampler had facing into the directional for almost all cases the higher concentrations. Although these studies coincide with

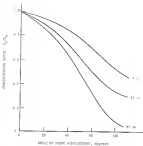


Fig. 7 Effect due to rearrangement of prods. in their chains (after Repland and Langewiesch, in Ref. [11]).

directional properties (1) and angular momentum (2) and the velocity of the central nucleon (3). In the calculations (4) (5) (6) (7) (8) (9) the particle size and the angle are neglected. The data sets of particle size and angle are important parameters. From stream velocity and stream diameter are not included in the analysis.

Figure (11) showed particles of 0.10, 0.15 and 0.20 mm diameter at flow speeds of 10, 20, 40 and 70 m/sec with the nuclei aligned over a range of angles from 0 to 120 degrees. It was used a trigonometric function to convert equation (1) to the form

$$A = 1 + 0.0001V_p \sin \theta + V_p \cos \theta V_p \sin \theta + V_p \cos \theta \quad (11)$$

This function only serves to invert the velocity ratio between 0 and 90 degrees and does not satisfactorily represent the physical properties of the flow stream. In fact, equation (11) becomes only an 0 degrees regardless of what the velocity ratio or particle size is. This suggests the fact since it has been shown that the concentration ratio will be high flow study and will decrease inversely proportional to the angle and particle diameter.

A more representative function can be derived in the following manner. Consider the coupling velocity V_1 to be greater than the target velocity V_2 . Let A_1 be the cross sectional area of the nuclei of diameter D_1 . The stream tube approaching the nuclei will have a cross sectional area A_2 such that

$$A_1 V_1 = A_2 V_2 \quad (12)$$

If (assuming) further (a4) is in the flow states, the projected area perpendicular to the flow is an ellipse with a major axis b_1 , minor (or) b_2 axis, and area $(b_1 b_2 \pi) \sin \theta / 4$. The projected area of the device would therefore be $b_1 \pi \sin \theta$ (see Figure 2). It can be seen that (1) the projected resistance is the value $\eta_0 \pi \sin \theta$ will occur the angle θ a function $f(\theta, A, B)$ of the particles in the volume $(b_1 + b_2) \pi \sin \theta / 4$ will leave the stream tube because of their inertia and will not occur the device. Therefore, with K_0 defining the actual concentration of the particles, the measured concentration in the device would be

$$C_0 = \frac{C_1 b_1 \pi \sin \theta}{A_1 \pi} = \frac{[1 - f(\theta, A, B)] (b_1 + b_2) \pi \sin \theta / 4}{A_1 \pi} C_1 \quad (13)$$

Using equations (1) and (13), this may be simplified to

$$A = C_1 K_0 = 1 + f(\theta, A, B) \sin \theta \quad (14)$$

$f(\theta, A, B)$ would be a function of both the velocity ratio B and the particle injection potential A as shown by Figure 2 and Figure (10). However, f will also be a function of the angle θ because as the angle increases, the velocity of the flow that the particles will enter is increased as also suggested.

It can be seen that for large values of Stokes number, B near unity, (a4) is for the predicted concentration ratio in equation (14) is much the theoretical limit of unity. The maximum error should theoretically occur somewhere between a Stokes number of 1 and 4 depending on the angle θ . The upper limit of $B = 4$ would be for an angle of 8 degrees in the critical regime in this chapter. The theoretical lower limit of $B = 1$

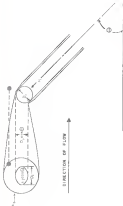


Figure 1. Rotating blade flow to control development and substantially simplify analysis

angle θ at an angle of 90 degrees in which case the particles would be traveling perpendicular to the nozzle. Since the nozzle has some frontal area relative to the flow stream, any particles that it collected must first travel into the nozzle. The average of this that a particle has to negotiate is how far the hole is taken the particle to traverse the diameter of the nozzle or d_p/n_p . Setting this equal to τ the time it takes a particle to change dimensions and rearranging terms, we obtain $\tau d_p/n_p = 1$ is the limiting condition for a particle to be able to take a turn into a nozzle positioned at a 90 degree angle to the flow stream. For angles between 0 and 90 degrees the maximum turn will occur between the limits of Stokes numbers of 1 and 0 and should be proportional to the average diameter of the frontal area of the nozzle. Fuchs [14] suggests that for small angles the scaling relationship will be of the form

$$S = 1 - 4 \sin^2(\theta/2) \quad (13)$$

Lefebvre [15] adapted a polylogarithmic correlation to an angle to the flow stream of 90 degrees for three submicron-sized molecules. By using a photoacoustic technique to make his he determined the accommodation coefficients for different sized molecules. From these divided over a range of Stokes numbers from 0.002 to 0.2 he developed the following empirical equation:

$$A = 1 - (0.002/n_p)^{0.5} \quad (14)$$

This equation can be used only in the range of Stokes numbers given and for a range in velocity ratios [8] from 1.45 to 4.45.

A longitudinal window in this case has a varying width. Because the detection collection of particle trajectories in a constant flow into a point that determines the viewing window is in a function of the source which generates and directs the coupling flow into and the first particle source. Figure 11) also indicates observed variation of source due to suboptimal coupling. To avoid a procedure involving an analog and a digital computer and measured losses in the present mechanism in the collection of the particulate matter. However, the results obtained by Figure are only for high values of Stokes numbers and are of little value for this study.

1. Source of the Material in Transport Flow

Although particulate coupling velocity is known to cause a particle coupling flow or source, there are also several other coupling source causing factors such as dust turbulence, aerosol forms factor (e.g., centrifugal, differential, gravitational or thermal) and particle alignment due to compression or dilatation flow. These factors are almost always present in an industrial process and cannot be assumed to be negligible. Not only do these factors cause coupling source directly but in addition they cause particulate concentration gradients and normal also distribution variations in which cause the source both in the radial and angular dimensions.

1. Source and Characteristics of Transport Flow

Transport flow in the transport flow is a direction other than that parallel to the dust source flow direction. In an air pollution

control volume, volume or control input data, is used as the primary

gibbs, continuity equation, momentum flow will occur, etc.

Flowing from the outlet of a system to a steady example is shown in Fig. 1. Flow and a well-recognized problem even for simple processes (e.g., simple). Sequential flow can also be caused by flow changes induced by changing (22). If the flow rate increases, the flow flows into the stack. Inexpensive, a balanced flow will occur (see Figure 9). Even if the flow occurs across the center of the stack, at the density flow field as volume or speed of magnitude of the stack flow rate, a steady volume flow process will occur (see Figure 10).

The velocity flow in the stack contains the characteristics of various series with fixed values along the stack axis. The gas velocity series is equal to balanced points in the stack. Hence this represents a free-flowing flow field, the swirl level changes and the velocity profile and static pressure distributions change with axial position along the stack. Swirl level is used here to represent the axial flow or transport rate of angular momentum (23). Velocity vectors at sequential or various flows are composed of axial, radial and tangential or circumferential velocity components (see Figure 11). The accelerated series flows are generally unsteady but during formation of the spreading flow the velocity is often distorted. The relative speed of magnitude of the velocity components varies across the flow field with the possibility of each one of the components becoming dominant at particular points (14).

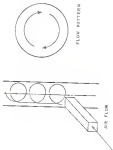


Figure 2. Temperature flow induced by rotation.

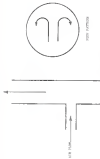


FIGURE 21 Flow reduction by an orifice



Figure 10. Flow fields in a rotating flow field

The two evidently different types of flow that are possible in a swirling flow field are taken as free vortex and forced vortex flow. In the swirling component of flow in free vortex in the cyclone unit, the tangential profile of the induced flow approximates that of a forced vortex. As the forced vortex flow moves along the axis of the stack, viscous stresses and losses occur at the wall which cause a reduction in the tangential velocity and dissipation of angular momentum. This loss of angular momentum is due to viscous action aided by unstable flow and fluctuating components. Simultaneously outside the boundary surface of the wall where inertial forces are significant, the fluid develops toward a state of constant angular momentum. This type of flow field with constant angular momentum is classified as free vortex flow. The angular momentum and tangential velocities of the flow from the jet stream flow up the stack [14].

Velocities and flow measured radial and tangential profile velocities distributions in a jet is an essential part in which swirling flow was produced by fluid mass [22]. The tangential velocity profiles and angular momentum distributions are plotted in Figures 11 and 12 from measurements taken at 1.24 and 2.5 diameters downstream of the origin of tangential flow. The tangential velocity W_t is made dimensionless by dividing it by the mean axial inlet velocity ($U_{0,0}$) as a pure vortex motion. These plots indicate developing flow fields, which are definite types of flow swirling. When approaching forced vortex flow in the nearest region of the pipe and flow approaching free vortex flow in the outer region. Further tests showed that the free vortex field



Figure 1: Three random variables X_1, X_2, X_3 (a, b, c) in a working ring (a, b, c)

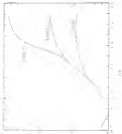


Figure 14. Energy spectrum of a many-body state.

development of (10) results in (11) which is the well known function (a plot of which is shown in Fig. 1) which is the profile of the radial velocity field in cylindrical coordinates in the initial conditions of the helix. Although no first flow was found in these tests, when it is shown that strong, periodic pressure oscillations occur in the helical region (11).

It should be noted that although tangential oscillations are higher in magnitude away from the axis of the pipe, the frequency is not as high after it changes the tangential velocity is still quite significant, due to the fact that the radial velocity. Therefore, although the EPR tested a requirement of coupling is that, therefore, detection of the source system (helical) will not eliminate the effect of coupling on tangential flow.

The angle of the flow relative to the axis of the pipe is related to the tangential component of velocity and is high as 90 degrees at some points in the flow. This component will be high enough that the coupling of velocity of system (11). Another interesting fact about the flow described in Figures 11 and 12 is that the radial profiles for the tangential component, $V_{\theta}/V_z = 0$ show that the velocity is still constant (11) as much as 1 inch. This indicates that the swirling flows are not necessarily symmetrical.

Effect of Helical Flow on Tangential Flow

Types of errors that could be expected to be introduced by tangential flow are: (1) errors in the concentration profiles and, (2) errors in the sampling error caused by non-isothermal flow.

described by the simplified theory, corresponding to the same time as shown previously. Thus, in the case of the results of the first two measurements, the values of the angle α of the wall of the stack, causing higher concentration in the water region.

Figure 11b) are taken at the outlet of a small industrial system to determine the magnitude of these three types of errors induced by cyclonic flow. Results of flow rates calculated at the different locations are presented in Table 1. As indicated by the data, various errors can result in terms of temporal flow. A maximum error of 11% occurred when the pilot tube was related to read a maximum velocity of 1.04. Depending position, to the stack, will also had a large error of about 10%. When coupling locations of the flow corresponding water. However, the error was reduced to 10%.

Tests performed at the same point but with different angle angles produced the data in Table 11. Measured flow concentrations was lower when the sampling probe was located at an angle of 0 degrees or parallel to the stack wall. The measured flow concentrations were found to increase at 10 and 30 degrees but then decreased at 60 degrees. Equation (10) shows that when counting at an angle, under constant atmospheric conditions ($\rho = 1.21$) the measured concentration will be less than the true concentration by a factor directly proportional to the angle. A constant concentration, which would be the true concentration, will occur as $\theta = 0$. When flow rate drops about 10% at an angle between 40 and 60 degrees to the axis of the stack. This can be confirmed by

Table 1
Table 1: Comparison of Model Performance Metrics

Model	Accuracy (%)	F1 Score (%)	AUC (%)
Model A (Baseline)	85	82	0.88
Model B (Proposed)	90	88	0.92
Model C (Ensemble)	88	85	0.90
Model D (DeepNet)	87	84	0.89

TABLE II
Continuum From 0 to 1: Heat and Strength Residuals/Layers

<u>Bonding Angle</u>	<u>Measured Conversion (100%)</u> <u>(mol/L) (mol/L)</u>
0	0.000
40	0.090
60	0.160
80	0.210

where Δt is the time interval, Δx is the distance between the two particles, and Δy is the distance between the two particles.

$$\Delta t = \frac{\Delta x}{v} \quad (4)$$

It is noted that Δt is the time interval, Δx is the distance, Δy is the distance, Δz is the distance, Δt is the time interval, Δx is the distance, Δy is the distance, Δz is the distance.

Table 10 gives the results of the numerical tests. Sampling with the results reported in the table will show an error of 10%.

Sampling at the edge of maximum velocity had reduced the error to 10%. The results cannot be compared directly to those with the smallest sampling approach because the first values were not the same due to equipment failure and equipment. Sampling in the straightened flow had a sampling error of 10%. It was expected that sampling at this location would give better results, but some of the particles were in period in the straightening zone and did not in the horizontal section of the duct. This means that from the flow stream.

Results of the distribution tests showed no significant effects of a concentration gradient across the turbine. This was due to the particles being too small to be affected by the aerodynamic force field set up by the moving flow.

4.2. Errors due to the 5-type pilot tube

The errors in the measurement of velocity and integrated calculations of this rate is important. They are due primarily to the existence of the turbulence used in error sampling. Because of the high particulate loading that much is correct sampling. Standard pilot tubes cannot be used to measure the velocity. Instead, the 5-type pilot tube must be used.

TABLE 111
 (continued)

<u>State, Division</u>	<u>Measured Balance</u> <u>July 1, 1967</u>	<u>Actual (ending)</u> <u>June 30, 1968</u>	<u>Change</u>
State (grants) with state aid	\$ 100	\$ 702	602
State-owned local agencies	\$ 104	\$ 102	(2)
Investment flow	\$ 207	\$ 207	0

Using the functional class of materials shown that will not plug (see Figure 1-2) enables the large pressure ratio to be an additional advantage of producing approximately a 35% higher differential pressure than the standard pilot tube for a given velocity. However, although the E-type pilot tube will give an accurate velocity measurement, it is somewhat insensitive to the direction of the flow (20-30). Figures 10 and 11 show the velocity versus flow rate and pilot angle. Although the E-type pilot tube is very accurate in pitch direction, the curve for yaw angle is unsmoothed and standard flow for an angle of 45 degrees in either direction. Because of this insensitivity to direction of flow in the yaw direction, the E-type pilot tube cannot be used in a tangential flow situation to align the nozzle to the direction of the flow, or to accurately measure the velocity in a particular direction.

The velocity in a rotational flow field can be broken up into three components at the axial, radial and tangential directions (see Figure 11). The magnitude of the radial and tangential components relative to the axial component will determine the degree of error induced in the tangential flow. Whether the radial or the tangential components of velocity affect the flow rate through the stack, will both affect the velocity measurement made by the E-type pilot tube because of their dimensional sensitivity. If the velocity velocity head were used to calculate the stack velocity, the resultant calculated flow rates and velocity heads could be off by as much as a factor of 1/2000. Aligning the probe parallel to the stack will reduce low rate dynamic flow errors because part of the radial and tangential velocity components will still be detected by the pilot tube



Figure 10. Refractive index vs. angle of incidence for an 8 mm plate (see text).



Figure 16: Inducting versus beam angle for 1.00 m and 1.24 m beams.

therefore, the speed U is not constant. In consequence, the rate of transport of the suspended fluid by radial velocity, U_r , the tangential velocity, U_θ , the angular velocity, U_ω , and the angle ϕ are to have the dimension:

4. Methods Available for Measuring Velocity Components at a Point (Fig. 1-2)

Almost all of the classical measurements of velocity components in a turbulent flow field have been based upon introduction of probes into the flow. Because of the insensitivity of various types to the introduction of probes, the probe dimensions must be small with respect to the velocity scale in order to minimally disturb velocity.

For various types of pressure probes capable of measuring velocity accurately are the Pitot and Pitot-static probes plotted in Figures 1-3a and b. The Pitot or three directional directional pressure probe is used to measure free jet and probe angles, and total and static pressure. Pitot pressure taps are drilled in a hemispherical or conical probe tip and on the side and at the pole of the tip, the other four spaced equidistant from the tip and from each other at an angle of 30 to 45 degrees from the pole. The operation of the probe is based upon the surface pressure distribution around the probe tip. If the probe is placed in a flow field at an angle to the flow then velocity vector that a pressure differential will be set up across those holes. The magnitude of which will depend upon the geometry of the probe tip. Accurate positioning of the probe and the magnitude and direction of the velocity vector. Such probes require calibration of the pressure



Figure 17b. Schematic diagram of a four-hole probe.

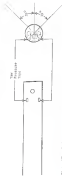


Figure 17a. Schematic diagram of a four-hole probe.



Figure 10 - Line with power only measured to tan angle (10)

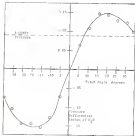


Figure 14. Reducing gross take variability to low angle (20)

The *Smith-Petersen* test, like all approaches to detecting nonlinearities, has a number of drawbacks. When applied to time series, it requires the behavior of the plant when tested to remain stationary, leading to improper conclusions. Errors in the DM test may also arise operating variations often occur during tests, and the sound of secondary flow effects generated by the loading of the gas stream. The prevailing conditions did not indicate any significant flow moving in the stack.

CHAPTER III
EXPERIMENTAL APPARATUS AND METHODS

1. EXPERIMENTAL DESIGN

General components of the aerosol flow system can be seen in Figure 2.

Figure 2. The aerosol system generated from a spraying atomizer consisted of the following major elements: (1) a spraying atomizer which was fed with a nebulizer solution where it was combined with diluent air. The air stream then flowed through a 10 in diameter PVC pipe containing, downstream, a nozzle. This was followed by a straight section of clear pipe from which samples were taken. The filter holder and nozzle used in a typical sample acquisition is shown following the straight section. The filter holder was attached into the duct as an angle from outside the box. A flow plate orifice, used to measure flow rate, followed the sampling box. A 1000 lpm industrial vacuum was used to move the air through the system. The flow rate could be controlled by changing the diameter of an orifice plate. An air by pass between the filter and the orifice plate was used as a flow adjust for the flow.

The sampling system (see Figure 3a) consisted of stainless steel clear solid metal connected to 1/2 in stainless steel ducts, filter holders. Each filter assembly was connected in series to a dry gas meter and a nebulizer, and drawn by an airstream pump with a by-pass valve to remove flow.

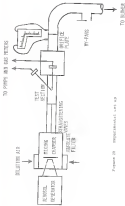


Figure 26. Experimental setup.

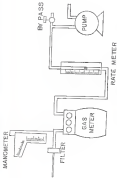


Figure 11. Schematic diagram.

2. Model description

2.1. System and geometry

A spinning disk surface generator (Fig. 2) was used to generate noncylindrical surfaces from 1.0 to 100 to 11.0 to 100 (mm high, etc). Disks were generated from a surface of 10° radius (a flatness of 0.01 mm) and 10° radius (a flatness of 0.01 mm) as a solution of free-form (a flatness of 0.01 mm) and up to 10° diameter/height (a flatness of 0.01 mm) used to show the particles could be detected by fluorescence methods (a flatness of 0.01 mm) and in the optical analysis of the particles. The surface of water and oil was allowed for a surface examination of the droplets. The droplets, containing chemical solutes, evaporated to yield particles whose diameter could be calculated from the equation

$$D_p = (C_p \cdot D_0) / D_0 \quad (1)$$

where

D_p = particle diameter, μ m

C_p = ratio of water volume to solvent volume plus water
volume (a flatness of 0.01 mm)

D_0 = original droplet diameter, μ m

It is of a known relationship whereby all three and liquid fuel were used. However, the size of the droplets produced were only dependent upon the (a flatness of 0.01 mm) of the chemical water mixture. Since the droplets are produced from a droplet (a flatness of 0.01 mm) between the (a flatness of 0.01 mm) and the surface

TABLE III
 SUMMARY OF DESCRIPTIONS OF SUPPLEMENTAL ADVERTISEMENTS

Original Description	Advertisement Schedule	% Exposure	Original Frequency, %	Number of Additional Exposures, %
A 100%	Optimum 10 sec	60	20.4	1.68
B 100%	Optimum 10 sec	60	20.2	1.27
C 100%	Optimum 10 sec	60	20.1	1.72
D 100%	Optimum 10 sec	60	20.3	2.62
E 100%	Optimum 10 sec	60	20.4	2.18
A 10%	Optimum 10 sec	60	20.2	1.15
A 10%	Optimum 10 sec	60	20.4	1.1
B 10%	Optimum 10 sec	60	20.2	1.66
B 10%	Optimum 10 sec	60	20.1	1.63
C 10%	Optimum 10 sec	60	20.6	1.8
C 10%	Optimum 10 sec	60	20.4	2.68
D 10%	Optimum 10 sec	180	22.4	8.8
D 10%	Optimum 10 sec	180	22.2	8.12
E 10%	Optimum 10 sec	60	20.3	11.1
Original Ad 1 sec	Normal Exposure	20.4	4.4	18.8

temperatures for deep and surface sampling of the ponding water samples. The surface sampling starts one hour prior to tapping and approximately 75% (see Fig. 1) ponding water. Differences of this large difference can be seen in Table IV where the densities produced were approximately 14% for the 1984 column and 12% for the 1985 column.

Before and after each run a sample of the particles was collected in a stainless disher and sized using a light microscope to take into account any slight variation in the performance of the spinning disc.

3. Reposed Polymers

In order to obtain large diskette numbers, reposed polymer was continuously dispersed by means of a rubber square ball into the water of the drum. The reposed polymer had a run of 15.0 gm.

5. Velocity Determination

The velocity at each sampling point was measured using a constant pressure tube. The flow was maintained constant during the test by maintaining the pressure drop across a thin-walled orifice placed in the system (20-25). Five orifice plates with orifice ranging in diameter from 1.5 to 7.5 mm were used to obtain a range of flow velocities of 0.1 to 0.40 m/sec (see Table V) in the 10 cm drum. To obtain higher velocities a 1 cm drum was used.

A typical velocity profile across the 1 cm drum plate was as presented in Table VI and plotted in Figure 11. The profile is

TABLE II
 RANGE OF RANGE-FINDING TESTS IN THE 100-1000

Range-Finder Model	As Range in 10^3 ft.	Range in Velocity m/sec.
1700	3.4 - 21.0	10 - 140
1720	3.3 - 21.0	140 - 100
1730	4.3 - 21.0	100 - 170
1740	4.1 - 22.0	160 - 100
175	1.2 - 14.0	100 - 1000

TABLE IV
OPTICAL VELOCITY TENSORS BY THE EXPERIMENTAL METHOD
(9.50 cm x 1.0" Tube)

Polarizer	Angle	Variations		Reproduced	
		Δn_{\parallel} on Δn_{\perp}	Δn_{\parallel} on Δn_{\perp}	Δn_{\parallel} on Δn_{\perp}	Δn_{\parallel} on Δn_{\perp}
1	0.544	1.17	1454	1.17	1444
1	0.546	1.18	1543	1.18	1441
1	0.550	1.20	1630	1.20	1438
1	0.554	1.23	1690	1.23	1435
2	1.504	1.34	1790	1.34	1433
2	1.506	1.37	1840	1.37	1431

Average Polarization (400/500)

90° Polar Tube Readings

1740

From Cell Plate 15

1425



Figure 12 Optical density profile as experimentally measured (O) and theoretically calculated (—)

with $P_{\text{max}} = 1.2$ (mm/sec) is obtained. The critical flow velocity U_{crit} is determined from the concentration $C = 1.1 \times 10^4$ (mg/l) (the maximum sedimentation rate) and is calculated to be 0.00012 (m/sec). The difference between the average velocity determined from the pilot tunnel and the critical plate velocities is probably due to the inability of the pilot tube to accurately measure velocity near the wall at points 1 and 2.

4. Selection of sampling points

Sakai (16) showed that the velocity profile corresponds almost across the diameter of a cylindrical duct, and that the magnitude of the concentration gradient varied with particle size. In order, for phase (a), therefore, the two sampling points were located symmetrically about the center of the duct at a distance of 2 cm from the center. Simultaneous concentric samples were taken at the two points and compared. Tests were repeated for different particle sizes. No concentration differences were found to exist at the two sampling points.

5. Sampling device

Two pairs of sampling nozzles were used from stainless steel tubing 0.0442 in. and 0.031 in. I.D. The nozzles were made approximately 12 in. long to minimize the effect of the disturbance caused by the filter holders in the flow at the entrance of the nozzles. Sakai (16) showed that a sharp edge profile was the most efficient design.

regions, the long, unobscured distance to a low gain factor and hence, an increase in the number of particles per field of view. The results from the probe and the results of sampling error and from the input results, the efficiency is affected by the relative cell thickness, the relative edge thickness and the angle of input. They were stated that if the edge thickness is less than 1/3 of the internal diameter and the angle is less than 11 degrees, then the variation in efficiency between due to particle removal could be less than 10. The results were designed accordingly.

1. Analytic Polyethylene

1.1. For Studies, Polyethylene

Various particles were obtained of Salomon type A glass fiber fibers. The fibers were then placed in a 100 ml beaker. One hundred milliliters of distilled water were then poured into the beaker held of the 100 ml beaker and then through the waste line to the beaker surrounding the fiber. The waste liquid concentration was then diluted and analyzed by a fluorometer (10).

1.2. For Studies, Polyethylene

The required point was collected on various fibers and analyzed under a microscope. In this part of the experiment the fibers and probe were analyzed separately. The fibers used for collecting the particles were 1.0 cm type 10 polyethylene fibers. In order to count the particles under a microscope a dark background was necessary,

thereafter, and (2) the gas flow rate and rate of pressure drop $\Delta P/\Delta t$ as the detected change being caused by the porous medium. The factors were adjusted until the minimum $\Delta P/\Delta t$ was obtained. If any background noise existed, this could lead to the $\Delta P/\Delta t$ value skewed and the nature area of the filter was incorrect.

The pollen sample on the active and filter holder was analyzed using impregnated slides and it is as you can tell from the figure with black grids. The impregnated was later observed several times to ensure background perturbations were gone. Once the background was low enough, the slides were placed onto the front half of the filter holder and through a microscope. The subject was then tracked through the microscope filter. The filters were allowed to dry and then the entire filter area was checked under the microscope.

5. Sample Procedure

1. Collected flow rate was obtained by installing an orifice plate and using the by pass as a flow adjust.
2. The orifice was measured using a standard pitot tube.
3. Minimum pressure solution was obtained for a given particle size.
4. Pressure rate collected on a uniform filter and rated using a light microscope.
5. A particle diameter which would allow for an isotropic sampling rate (about 10 μ m) was selected.
6. Isotropic sampling rates were calculated and sampling flow rates were adjusted accordingly.



Figure 10.10: Equipment setup for measuring vertical distance using theodolite and leveling staff.

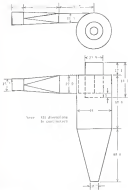


Figure 8. Car body used in the study in gasless welding class



Figure 5. Photograph of the 3-dimensional plate with its surrounding well. (Left) Shows the location of the previous tags.

radius of the fibre perpendicular to the axis of the nozzle, and tangent to the shock wall. The pitch angle is a measure of the flow perpendicularity to the axis of the shock and perpendicular to the shock walls. The axial component of the velocity can therefore be determined from the following equation:

$$V_a = V_t \cos \theta \quad (10)$$

where V_a = component of velocity flowing parallel to the axis of the shock

V_t = total or resultant velocity measured by the pitot tube

θ = $90^\circ - \alpha$ (see fig. 1 and text)

CHAPTER 2 FIBERS AND BLENDS

1. General Statistical Approach

1.1. Brown Motion

Suppose we have set up and run with fiber a new random copolymer variable. Our velocity would fluctuate and produce ~~fluctuations~~ in order to produce a range of fiber values from 0.00% to 1.00%. The Brown motion used in the analysis of this was calculated from

$$s = \frac{C_1 \cdot T \cdot \Delta t}{\sqrt{C_2 \cdot T \cdot \Delta t}} \quad (10)$$

where

$$C_1 = 1.477 \times 10^{-4} = 1.47 \times 10^{-4} \cdot (10^{-10} \cdot 10^{-10}) \quad (11)$$

and

$$C_2 = \text{area from graph} = 0.044 \text{ cm} \quad (12)$$

where the density and viscosity used in the calculations were

$$\eta = 1.44 \times 10^{-4} \text{ g/cm sec} \quad (13)$$

$$\rho_p = \text{density of unswollen polymer} = 1.275 \text{ g/cm}^3 \quad (14)$$

$$\rho_f = \text{density of exposed polymer} = 1.1 \text{ g/cm}^3 \quad (15)$$

6. Sampling with Filtered Particles

In order to determine if the concentration of particles was the same at both sampling locations, simultaneous samples were taken with both samplers aligned parallel to the flow. Table VII shows the results of counts performed over a range of Stokes numbers from 0.003 to 0.75. The average over all of the counts showed only a 0.34% difference between the two points with a 95% confidence interval of 11.3%. The data show an increase in the range of the counts as the Stokes number increases. This can be expected because a small error in probe misalignment would have a greater effect at the higher Stokes number.

7. Analysis of Probe Loss

In the analysis of the spray using tapered probes, the filter (Wet) and probe wash were measured separately. This section allowed for the determination of the importance of sampling with the filter (Wet) and. From Table VIII it can be seen that even for a solid dry particle, analysis of the probe wash is a necessity. An average of 49% of the particles entering the probe was collected in the walls of the nozzle-filter holder assembly. This was only for particles aligned parallel to the flow stream and sampling radially inward. Therefore, the loss of particles was due to turbulent deposition and possibly bounce off the filter and probably not inertial impaction. For cases run with the nozzle at an angle to the flow stream, it is assumed that the loss would increase as separation of particles at the walls became

TABLE 5
EFFECTS OF PARTICULATE MATTER CONCENTRATIONS IN THE FRESH WATER
FOR NOCTUIDS REARED ON THE FRESH STREAM

PM10 (mg/L)	PM2.5 (mg/L)	PM10 (mg/L)	PM2.5 (mg/L)
5.0	0.01	10.0	0.02
10.0	0.02	20.0	0.04
15.0	0.03	30.0	0.06
20.0	0.04	40.0	0.08
25.0	0.05	50.0	0.10
30.0	0.06	60.0	0.12
35.0	0.07	70.0	0.14
40.0	0.08	80.0	0.16
45.0	0.09	90.0	0.18
50.0	0.10	100.0	0.20
55.0	0.11	110.0	0.22
60.0	0.12	120.0	0.24
65.0	0.13	130.0	0.26
70.0	0.14	140.0	0.28

PM10 and PM2.5 represent the amount of suspended particulate matter

important. Therefore, to gain the accurate value of the degree of the loss of material (LMA) in the filter and with all that in the series.

The probe loss for eight tests using 8 ° (inverted position) was also studied separately for comparison with the results of the original probe tests. While pouring sample, from 11 to 34% of the total mass was collected in the waste and feed out of the filter holder. While this was somewhat less than the amount of required probe loss found in the waste, it is potential enough to show the importance of installing the waste tank with the filter tests. Also because of the variation of the amount collected in the waste during identical tests the probe loss should be accounted for by a correction factor. During further testing, it was qualitatively observed that the percent in the probe waste increased with particle size and decreased with increasing waste diameter.

3. The Effect of Waste Characteristics on Sampling Efficiency

The separation coefficient was determined by comparing the amount of particles either captured while sampling horizontally with a vertical waste placed parallel and a new waste set at an angle to the flow stream. Tests were run at three angles: 10, 45 and 90 degrees. The results showed the theoretical predictions in its pure manner for all three angles the separation coefficient approached 1 for small Stokes numbers (St), decreased as St increased and then leveled off at a minimum of one for large values of Stokes number. The most significant changes occur in the range between $St = 0.01$ and $St = 1.0$.

TABLE VI
PERCENT OF PARTICULATE MATTER OBSERVED IN THE WINDY PERIOD
FOR SITES OF AN OCEAN OF AN OCEAN (1971-1972) (1971-1972)

<u>Site No.</u>	<u>Site No.</u>	<u>Site No.</u>	<u>Site No.</u>
100	111	122	133
144	155	166	177
188	199	200	211

Percent represents the number of windless periods observed

Figures 19, 20 and 21 represent the coupling efficiency as a function of Stokes number for 30, 40 and 50 degrees respectively. The experimental data used in these plots/tables are in Tables I, II and III. From these tables it can be seen that the correlation of particle diameter and velocity and nozzle diameter were worked earlier randomly. This was done to check the legitimacy of using Stokes number as the principle independent variable. From the shape of the curves in Figures 20-24, it can be seen that the explosion coefficient is indeed a function primarily of Stokes number.

The curves for 30, 40 and 50 degrees are all similar in shape except for the values of Stokes number where they approach their theoretical limit. At the angle of misalignment interested, the rate slightly the explosion coefficient reaches its maximum value. This can be accounted for as an apparent change in nozzle diameter. Because θ is the only parameter in the Stokes number that is affected by the nozzle angle to the flow stream. As expected before, the nozzle diameter is important because it determines the amount of time available for the particle to change direction (approximately $\pi \rho_p / \rho_g U_0$). As the nozzle is tilted at an angle to the flow stream, the projected frontal area and therefore the projected nozzle diameter are reduced proportional to the angle. Therefore as the angle of misalignment increases, the time available for the particle to change direction decreases leading to increased coupling noise for a given value of \bar{U} . To normalize these curves for angle to the flow stream, it is necessary to define an adjusted Stokes number St' which takes into account the change in projected



Figure 26. Sampling efficiency vs. station number at 100 m. (continued)



Figure 2: Sampling efficiency as a function of the number of samples. The solid line represents the sampling efficiency and the dashed line represents the sampling error.



Figure 26. Damping effect of a student making an error.

TABLE 1
 Variation coefficient as a function of grade

Index number ref/2014	Article number in collection	Grade boundary in		Grade boundary	Grade
		mm			
170	1 00	0 00	0 00	0 00	0 00
180	1 00	0 00	0 00	1 00	0 00
190	1 00	0 00	0 00	0 00	0 00
200	1 00	0 00	0 00	0 00	0 00
210	1 00	0 00	0 00	0 00	0 00
220	1 00	0 00	0 00	0 00	0 00
230	1 00	0 00	0 00	0 00	0 00
240	1 00	0 00	0 00	0 00	0 00
250	1 00	0 00	0 00	0 00	0 00
260	1 00	0 00	0 00	0 00	0 00
270	1 00	0 00	0 00	0 00	0 00
280	1 00	0 00	0 00	0 00	0 00
290	1 00	0 00	0 00	0 00	0 00
300	1 00	0 00	0 00	0 00	0 00

Category	Variable	Value	Unit	Notes
Economic	GDP	1200	Billion USD	2019
	Unemployment	5.2	%	2019
Social	Population	100	Million	2019
	Life expectancy	75	Years	2019
Environmental	CO2 emissions	150	Million tons	2019
	Renewable energy	10	%	2019
Health	Hospital beds	500	Per 1000	2019
	Healthcare spending	8	% of GDP	2019

TABLE 11
 SUSPENSION CONCENTRATION AS A FUNCTION OF SPAN FOR 100% POLYMERIZATION

Polymer concentration	Polymer concentration percentage	Residue Polymer		Residue Polymer	Polymer concentration
		%			
1.00	1.00	0.100	0.100	0.100	100.0 100.0 100.0
1.00	1.25	0.100	0.100	0.100	100.0 100.0 100.0
1.00	1.50	0.100	0.100	0.100	100.0 100.0 100.0
1.00	1.75	0.100	0.100	0.100	100.0 100.0 100.0
1.00	2.00	0.100	0.100	0.100	100.0 100.0 100.0
1.00	2.25	0.100	0.100	0.100	100.0 100.0 100.0
1.00	2.50	0.100	0.100	0.100	100.0 100.0 100.0
1.00	2.75	0.100	0.100	0.100	100.0 100.0 100.0
1.00	3.00	0.100	0.100	0.100	100.0 100.0 100.0
1.00	3.25	0.100	0.100	0.100	100.0 100.0 100.0
1.00	3.50	0.100	0.100	0.100	100.0 100.0 100.0
1.00	3.75	0.100	0.100	0.100	100.0 100.0 100.0
1.00	4.00	0.100	0.100	0.100	100.0 100.0 100.0
1.00	4.25	0.100	0.100	0.100	100.0 100.0 100.0
1.00	4.50	0.100	0.100	0.100	100.0 100.0 100.0
1.00	4.75	0.100	0.100	0.100	100.0 100.0 100.0
1.00	5.00	0.100	0.100	0.100	100.0 100.0 100.0
1.00	5.25	0.100	0.100	0.100	100.0 100.0 100.0
1.00	5.50	0.100	0.100	0.100	100.0 100.0 100.0
1.00	5.75	0.100	0.100	0.100	100.0 100.0 100.0
1.00	6.00	0.100	0.100	0.100	100.0 100.0 100.0
1.00	6.25	0.100	0.100	0.100	100.0 100.0 100.0
1.00	6.50	0.100	0.100	0.100	100.0 100.0 100.0
1.00	6.75	0.100	0.100	0.100	100.0 100.0 100.0
1.00	7.00	0.100	0.100	0.100	100.0 100.0 100.0
1.00	7.25	0.100	0.100	0.100	100.0 100.0 100.0
1.00	7.50	0.100	0.100	0.100	100.0 100.0 100.0
1.00	7.75	0.100	0.100	0.100	100.0 100.0 100.0
1.00	8.00	0.100	0.100	0.100	100.0 100.0 100.0
1.00	8.25	0.100	0.100	0.100	100.0 100.0 100.0
1.00	8.50	0.100	0.100	0.100	100.0 100.0 100.0
1.00	8.75	0.100	0.100	0.100	100.0 100.0 100.0
1.00	9.00	0.100	0.100	0.100	100.0 100.0 100.0
1.00	9.25	0.100	0.100	0.100	100.0 100.0 100.0
1.00	9.50	0.100	0.100	0.100	100.0 100.0 100.0
1.00	9.75	0.100	0.100	0.100	100.0 100.0 100.0
1.00	10.00	0.100	0.100	0.100	100.0 100.0 100.0

Table 1: Summary of data

Category	Sub-category	Value	Unit	Source
1.1	1.1.1	100	kg	100
1.2	1.2.1	200	kg	200
1.3	1.3.1	300	kg	300
1.4	1.4.1	400	kg	400
1.5	1.5.1	500	kg	500
1.6	1.6.1	600	kg	600

TABLE III
 ACTIVATION CORRELATION AS A FUNCTION OF PRESSURE AND OF MOLECULAR WEIGHT

Polystyrene molecular weight	Intrinsic viscosity in benzene	Number of moles of initiator	Pressure, mm. Hg.	Relative rate of polymerization	Relative viscosity
100	1.12	0.10	0.10	0.001	0.001
100	1.10	0.10	0.10	0.001	0.001
100	1.12	0.10	0.10	0.001	0.001
174	1.15	0.10	0.10	0.001	0.001
156	1.15	0.10	0.10	0.001	0.001
156	1.15	0.10	0.10	0.001	0.001
156	1.15	0.10	0.10	0.001	0.001
156	1.15	0.10	0.10	0.001	0.001

Table 1: GAT (continued)

Indexing JNT/JST	Processing P/JNT/JST	Results R/JNT/JST	Analysis A/JNT/JST	App. mem. C/JNT/JST
100%	5.00	0.400	0.11	10.0 10.0 10.0
10%	4.00	0.400	0.50	10.0 10.0 10.0
10%	1.00	1.000	1.00	10.0 10.0 10.0
10%	0.200	0.200	0.20	10.0 10.0 10.0
10%	5.00	0.400	0.10	10.0 10.0 10.0
10%	1.000	1.000	1.000	10.0 10.0 10.0

with following σ^2 value: then a least squares $1/\sigma^2$ (homoscedastic) coefficient for (6) (5) and (6) degree curve patterns (see Figure 10) found to be, respectively, the same (66) and one-half (33) (most likely) quadrupled coupling velocities and Figure 12.

Repeating the experiment below the Stefan surface, it was observed to give as a function of θ the value of λ where the expansion coefficient reached a value that represented 75% of the maximum. For example the maximum theoretical curve for 40 degrees is 0.00050 at $\lambda = 1$. Therefore the value of λ of interest is where there is a 0.000375. If its coupling error is an expansion coefficient of $1 \pm .45 = .55$ for 40 degrees, equations (7) and (10) were solved for $\theta = 40^\circ$ and $\lambda = 0.55$ to obtain a value of $\lambda = 5.8$. This velocity tells not only known are theoretical maximum coupling error is 0.5, the same as for all degrees. The values for 60 and 70 degrees were obtained from Figures 17 and 18 respectively. Because of the flatness of the 70 degree curve (6) curves only 1/4 inch rise and a half inches of magnitude of λ , it was not possible to locate exactly when the curve reached 75% of its maximum value. Therefore an error for 70 degrees was used in this analysis.

The equation for the adjusted Stefan surface determined from Figure

10 is

$$y = 2x^2 + 0.0019 \quad (17)$$

Using this equation it can be determined that the Stefan numbers for 40 and 70 degrees must be multiplied by 1.54 and 7.76 respectively, to account for the effect of angle on the Stefan curve on the

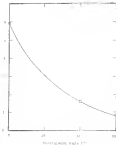


Figure 75. Number of correct responses as a function of the number of trials.

approximate results (Gaussian). Using these approximation factors it is possible to use the data to determine an expression for H^* in equation (10). Setting $k = 1$ and solving for H^* this equation becomes

$$H^*(H^*) = \frac{H_0 + H_1}{2(H_0 + H_1)} \quad (12)$$

Using this expression the experimental data were used to plot H^* as a function of the adjusted factor number H (see Figure 14). From this plot, it can be observed that the data points for 10, 15 and 20 degrees all fall approximately on the same line. It should be noted that most of the variance is due to the 10 degree data and that the amount of the variance is somewhat irregular. Solving equation (12) for 10 degrees, implies that the coupling factor (10-15) must be multiplied by 1.5 in addition to with the 10 degree data. This has an effect of greatly decreasing any spread in the experimental data.

In deriving a model for laminated coupling lines it was necessary to develop an expression for the loss across through the layer in Figure 10. An equation of the form similar to that used by Indigoro and Gerson was selected to fit the data.

$$H^*(H^*, H) = 1 - \frac{1}{1 + \alpha H} \quad (13)$$

where α will be the constant. The advantage of this equation form is that it will transfer to the theoretical expressions of the relationship to $H = 0$ approaches zero for very small values of H and approaches 1 for very large values of H .²



Figure 10. $\log R_a$ vs. adjusted radius number for 10 and 20 degrees.

which corresponds to determine the constants a and b . It was found that the roots of the equation had to be a pure number, to allow k^2 to approach 1 at a faster rate for values of k^2 greater than 0.5. The following is the final form of the equation obtained:

$$F(k^2, \theta) = 1 - \frac{1}{(1 + 0.67\theta)^2} \exp \quad (25)$$

The constants were determined through trial and error to be 0.66 and 0.65 for a and b respectively. Therefore, the final equation to describe the coupling efficiency due to mode mismatch is a function of degrees of freedom parameter $k = 1$:

$$k = 1 + \{ \text{part of } F(k^2, \theta) \} F(k^2, \theta) \quad (26)$$

where

$$F(k^2, \theta) = 1 - \frac{1}{(1 + 0.67\theta)^2} \exp \quad (27)$$

and

$$k = 1 + \exp \{ \text{part of } F(k^2, \theta) \} \quad (28)$$

The F equations are valid for $0.5 \leq \theta \leq 10$ degrees and k between 1 and infinity. In Figure 11, it can be seen from the graph that the equation on the right of this represents accuracy. Figure 12 is a plot of the coupling efficiency due to mode mismatch between k and k_0 degrees as k degree increases.

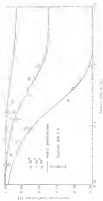


Figure 11. Dependence of the equilibrium constant on the logarithm of the activity of the reactants. The solid, dashed, and dotted lines are the results of the model calculations. The open circles with vertical bars are the experimental data.

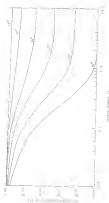


Figure 27. Normalized frequency f/f_0 versus normalized time t/T_0 for various series numbers.

To derive the immediate quantitative impact of α it is necessary to take into account the combined effect of both a money shock and a technology velocity shifter from the first period velocity. The theoretical model predicts that the timing efficiency will be as the first

$$k = 1 + (\text{short} - \alpha) \quad (38)$$

where

$$k = \frac{\partial \log \lambda}{\partial \log \alpha} \quad (39)$$

Since the reduction of expected money growth due to money growth will affect the long velocity for a particular exchange rate, when sampling at an asymptotic velocity, the algebraic factor under α should also be used in the equation for k as well as β .¹⁰ Another verification that can be made in the model involves assuming for the fact that $\partial \log \lambda / \partial \alpha$ does not equal 1 when $k = 1$.

$$\frac{\partial \log \lambda}{\partial \alpha} (k = 1) = 1 - \frac{1}{1 + \frac{1}{\alpha} \frac{\partial \log \lambda}{\partial \log \alpha}} \quad (40)$$

To measure the effect of α on k will be decided by $\partial \log \lambda / \partial \alpha$ so that equations (38) and (39) are valid at $k = 1$. The effect on the second two factors

$$k = 1 + (\text{short} - \alpha) \frac{\partial \log \lambda}{\partial \log \alpha} \quad (41)$$

It can be seen again to be an obvious first in the model is that the dispersion coefficient equals 1 because $k = 1$ is independent of the

floats surface. An example of that is when $\beta = 1.000$ or $\beta = 0.999999$. This phenomenon can be explained as follows. Assume the propeller float at the centre of the needle is one half the needle (and string) diameter (0.00125 m), its cross section is negligible, each cross-section is 40 slices composed of circular disk into the needle. The sample velocity must be one half of the free stream velocity or $U = 1$. Therefore, the resolution of $U = 1.00000$ defines the resolution for obtaining a representative sample when the needle is elongated with the flow stream.

Since the sampling mechanism used to determine $f(U, H)$ and $\beta(U, H)$ were substantially different (photographic microscope vs computer mapping) it was necessary to see if the two methods gave comparable results before the data could be tested. Four sets of seven were run with two parallel needles, the control needle sampled continuously and the test needle sampled discontinuously. Tests were performed at two Stokes numbers ($St = 0.024$ and $St = 0.178$) and at two velocity ratios ($H = 1.5$ and $H = 0.511$). The regression coefficients obtained by comparing the two methods independently are presented in Figure 11 and Table III. The data showed the width of the experimental bands of the lines produced does depend on Lewis's data [Equations (9), (9) and (14)].

Since the two methods give comparable results, experiments were run to test the model. A control needle was placed parallel to the flow stream and the sampling velocity was set to be identical. The test needle was inserted at an angle from outside the duct and the sampling velocity was set to be either one half or two times the duct



Figure 10. Concentration of a substance A with respect to position (cm) (100)

1932-1933

Comparison of Actual Production with 1932-33 Actuals (in thousands of bushels)

Production in 1932-33 (thousands)	Actual Production (thousands)	Actual Production (thousands)	Actual Production (thousands)	Total Actual Production (thousands)	1932-33 Actual (thousands)
4.7	1076	1076	1076	1076	1076
5.3	1076	1076	1076	1076	1076
6.2	1076	1076	1076	1076	1076
1.1	1076	1076	1076	1076	1076

class molecule. Tests were run for a range of fusion numbers from 0 to 1. This range was selected because this was expected to be the area where the greatest change in equilibrium coefficients occurred. The data obtained for $k = 1$ and $k = 0.5$ for a 40 degree molecule are presented in Tables XIV and XV. These data are plotted and compared with the model prediction in Figure 14. The equilibrium coefficients here indeed appear to be unity when $k = 1$ and to be on the order of $k + 1$ and $k + 0.5$ degrees. The data for $k = 0.5$, $k = 40$ degrees appear to approach theoretically (100) at about 15-20% or approximately a value of fusion number of 0.5 to 1. This is near the location that the equilibrium coefficients for $k = 40$ degrees, $k = 1$, intersect the theoretical limit. This further confirms the accuracy of using an adjusted fusion number when the probe is also aligned with the flow stream.

To further test the model, experiments were run at 40 degrees ($k = 0.5$ and $k = 0.2$) and at 10 degrees ($k = 1, 0.5$). These data presented in Tables XVI and XVII are plotted in Figures 15 and 16 and also show good agreement with the prediction model.

These tests were run at $k = 40$ degrees, $k = 1.5$ and $k = 0.1$ (see Table XVIII), an average equilibrium coefficient of only 1.25 was obtained. The value predicted for equation (14) for these conditions is 40%. It appears that the model fails apart at 40 degrees for $k \neq 1$. This is due to the fact that when $k = 40$ degrees, there is more projected frontal area of the probe. Thus means that unnecessarily sampling would be no any probes or detectors in examination or it does when perturbation for as great of the projected area were. Because of this it is necessary to get the condition $k = 40$ degrees in equation (24).

[illegible]

University acronym	Fertilizer Transfer Efficiency	Ratio to Biomass -%	Ratio, Root:Leaf	Significance level, P < 0.05
UO	4.46	0.003	0.002	0.001
UO	0.0	0.003	0.002	0.001
UO	0.0	0.003	0.002	0.001
UO	0.0	0.003	0.002	0.001
UO	0.0	0.003	0.002	0.001

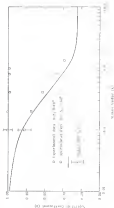


Figure 10: The relationship between the number of nodes (N) and the number of edges (E) in a network.

TABLE 1
 SUMMARY OF RESULTS FOR THE ANALYSIS OF THE DATA FROM THE STUDY OF THE EFFECT OF THE TYPE OF THE SUBSTRATE ON THE GROWTH OF THE CULTURE

Substrate	Sample of substrate	Initial biomass	Final biomass	Yield (%)	Specific growth rate (1/h)
101	0.1	0.100	0.100	100	0.100
101	0.2	0.100	0.100	100	0.100
101	0.3	0.100	0.100	100	0.100
101	0.4	0.100	0.100	100	0.100
101	0.5	0.100	0.100	100	0.100
101	0.6	0.100	0.100	100	0.100
101	0.7	0.100	0.100	100	0.100
101	0.8	0.100	0.100	100	0.100
101	0.9	0.100	0.100	100	0.100
101	1.0	0.100	0.100	100	0.100

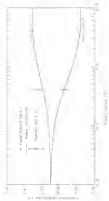


Figure 10. Coupling efficiency vs. Bragg angle at $\lambda = 633$ nm for $\theta = 0.5^\circ$ and 0.7° .



Figure 10: Variation of the ratio of the maximum value of the normalized velocity profile to the maximum value of the normalized velocity profile at the inlet, denoted as U_{max}/U_{inlet} , versus the normalized axial distance z/L .

TABLE VIII

ANALYTICAL DATA FOR POLYMERIZATION OF MONOMER 10A

Polymer Yield, %	Intrinsic Viscosity in CH ₂ Cl ₂	Elemental Analysis		Degree of Substitution, \bar{x}
		Calcd	Found	
100	0.5	61.10	61.10	1.0

Although the experimental data for 30 degrees do not agree well with the predictions until they do agree favorably with the original equation of Lohmann (26) [equation (24)]. For the conditions of $\theta = 0.00$ and $k = 2.1$, his equation predicts an expansion coefficient of 1.09. This comparison is closer than could be expected considering the fact that two completely different cooling schemes were used, and Lohmann did not analyze the nature of perturbations reflected in the probe.

It should be pointed out that the term for T^2/P^2 does not appear in eq. (8). This means that equation (8) will not be equal to Lohmann and Lohmann's preceding equations (26), (27) and (28) and therefore equation (10) should not be used for $\theta = 0$.

3.2. Temperature, Time, Cooling

Eight thermocouples placed for the velocity measurements were collected according to 1% (total) 1-17 (see table 12). Measurements were made using the 1-hole pilot tube at three equal distances from the inlet (25, 50, 75, 100 and 125 diameters) to the center of the duct. At each point in the traverse, the pilot tube was removed until the pressure differential between pressure taps 3 and 4 (see Figure 20) was zero. This angle was recorded as the yaw angle and the pressure readings from all five pressure taps were recorded for later calculation of yaw and roll pressures and pitch angle.

During the initial velocity traverse, a duct zero was determined in the center of the duct where the direction of the flow could not be determined with the pilot tube. The zero was not characterized by negative readings at all five pressure taps which did not cover most

Table 10
LOCATION OF SURFACE POINTS

Point	S. of Boundary	Distance from (Point 10)
1	5.5	0.05
2	10.4	0.07
3	19.4	0.05
4	21.3	0.11
5	43.3	11.34
6	59.4	24.93
7	69.5	37.67
8	76.7	50.09

NOTE: Boundary = 10.75 mi

with the rotation of the probe. Inside the 4000-4000 Å range not possible to determine the direction of flow because there was no point in the 180 degree rotation of the probe where the pressures at point 1 and 3 were the same. The location of the rays were not measured at each location along the duct axis and recorded. During the velocity measurements, it was observed that the flow was very sensitive to downstream disturbances & resulted at the end of the pipe produced large fluctuations in the pressure measurements.

Figure 11 shows the graphical interpretation of the patch and ray components of velocity. The ray radii r_1 and r_2 represents the distances from the center of the duct to the outer boundary of the rays. Figure 12 shows the flow region was approximated by the following equation:

$$A_{flow} = \frac{\pi(r_1^2 - r_2^2)}{2} \quad (6)$$

Table III lists the calculated results of the velocity vector results at the flow inlet pressure. The low flow was the flow measured when a restriction was placed at the inlet of the blower. The restriction reduced approximately a 45% decrease in the flow rate. The high flow rate represented a relatively flow rate of 35,000 liters per minute, and the low flow rate was 11,200 liters per minute. The Reynolds number of the system calculated at a basis of the average axial flow rate were 30,000 and 10,000 for the low and high flow rates respectively.

After the data collection was done, it appeared that flow flow points number 1 did not agree well with the rest of the pressure points. Upon

TABLE 1A
 1970-8000 PPM FOR NEGATIVE- δ S
 (a) 1-DIGITIZED REPRESENTATION OF THE CURVES

1-8 Low Flow

Point	Discharge, m^3/sec			Total Velocity (m/sec)	Depth to top of sediment (m)	Fugacity factor (%)
	Front	Top	B			
1	---	---	---	---	---	---
2	18.5	27.5	15.1	2764	408	14.04
3	27.5	37.5	18.0	3663	507	13.61
4	---	---	---	---	---	---
5	37.5	75.0	75.0	3245	544	15.25
6	45.0	60.0	41.1	1743	447	13.25
	58.0	34.0	37.3	1762	444	15.47
7	52.0	44.0	33.4	1440	441	10.07

1-8 High Flow

Point	Discharge, m^3/sec			Total Velocity (m/sec)	Depth to top of sediment (m)	Fugacity factor (%)
	Front	Top	B			
1	---	---	---	---	---	---
2	24.4	64.0	44.4	2723	113.0	13.90
3	34.4	76.0	72.3	2348	144	13.33
4	---	---	---	---	---	---
5	4.0	18.4	14.4	1896	144	10.78
6	20.0	41.4	37.0	1609	144	14.03
7	27.0	47.4	40.0	2140	133.1	20.08
8	37.0	34.4	33.25	2017	127.3	20.84

--- Indicate 1 has not come to the wall to either downstream of all five 1980-8000 ft.

--- Indicate that inside the negative pressure section

TABLE VII
 FIVE-PORT TEST TUBE CHARACTERISTICS
 BASED ON 2 PLASMA CONDENSERS OF THE CURRENT

1-5 Low Flow

Flow, cm/sec.	Angles, degrees			Total Reflector Pressure, mm/Hg.	Anode Velocity cm/sec.	Temperature mm/Hg.
	Left	Top	Right			
0	0	0	0	0	0	0
10	10.0	10.0	10.0	1700	190	1120
20	20.0	20.0	20.0	1400	440	1030
30	30.0	30.0	30.0	1100	890	1040
40	40.0	40.0	40.0	850	1340	1010
50	50.0	50.0	50.0	600	1790	970

1-5 High Flow

Flow, cm/sec.	Angles, degrees			Total Velocity mm/Hg.	Anode Velocity cm/sec.	Temperature mm/Hg.
	Left	Top	Right			
0	0	0	0	0	0	0
10	10.0	10.0	10.0	1200	1000	1110
20	20.0	20.0	20.0	1150	1500	1150
30	30.0	30.0	30.0	1100	2000	1080
40	40.0	40.0	40.0	1050	2500	1000
50	50.0	50.0	50.0	1000	3000	950

(1) Data for 1 was the same as the data for other locations of all the previous pages.

(2) Data from opposite the negative pressure section.

(3) This high value can probably be attributed to one of the peak pressure tubes measuring less the negative pressure area.

TABLE 11-1
 TYPICAL TEST-TUBE MEASUREMENTS
 OF 2-D BENTON CONFINEMENT OF THE FLOODGATE

Test No.	Applied, kN/m ²			Total Settlement mm/m ²	Applied Settlement mm/m ²	Remaining Settlement mm/m ²
	Depth, cm	Angle, deg	β			
1	0.0	0.0	0.0	0.00	0.00	0.00
2	20.0	0.0	0.0	1.00	0.00	0.99
3	10.0	0.0	0.0	1.00	0.00	0.99
4	0.0	10.0	0.0	1.00	0.00	0.99
5	0.0	0.0	0.0	0.00	0.00	0.00
6	10.0	0.0	0.0	1.00	0.00	0.99
7	20.0	0.0	0.0	1.00	0.00	0.99
8	20.0	10.0	0.0	1.00	0.00	0.99

2-D High Flow

Test No.	Applied, kN/m ²			Total Settlement mm/m ²	Applied Settlement mm/m ²	Remaining Settlement mm/m ²
	Depth, cm	Angle, deg	β			
1	0.0	0.0	0.0	0.00	0.00	0.00
2	20.0	0.0	0.0	0.00	0.00	0.00
3	10.0	0.0	0.0	0.00	0.00	0.00
4	0.0	0.0	0.0	0.00	0.00	0.00
5	0.0	0.0	0.0	0.00	0.00	0.00
6	10.0	0.0	0.0	0.00	0.00	0.00
7	20.0	0.0	0.0	0.00	0.00	0.00
8	0.0	0.0	0.0	0.00	0.00	0.00

— Test No. 1 was run close to the wall to allow inspection of test tube location logs.

— FLOOD tests include the negative pressure section.

TABLE 13-12
 1970-1980 FUEL TONNAGES
 (a) 1. STATIONARY/STATION OF THE CRUISE

0-0 Low Flow

Point	Engine, Degrees			Total Fuel (lb) /hour	Total Fuel (lb) /hour	Temperature /hour
	Low	High	0			
1	---	---	---	---	---	---
2	30.0	30.0	30.0	1434	1434	179.1
3	30.0	30.0	30.0	1434	1434	179.1
4	---	---	---	---	---	---
5	0.0	30.0	30.0	1434	1434	179.1
6	30.0	30.0	30.0	1434	1434	179.1
7	30.0	30.0	30.0	1434	1434	179.1
8	30.0	30.0	30.0	1434	1434	179.1

0-0 High Flow

Point	Engine, Degrees			Total Fuel (lb) /hour	Total Fuel (lb) /hour	Temperature /hour
	Low	High	0			
1	---	---	---	---	---	---
2	30.0	30.0	30.0	1434	1434	179.1
3	0.0	30.0	30.0	1434	1434	179.1
4	---	---	---	---	---	---
5	0	30.0	30.0	1434	1434	179.1
6	30.0	30.0	30.0	1434	1434	179.1
7	30.0	30.0	30.0	1434	1434	179.1
8	30.0	30.0	30.0	1434	1434	179.1

1970-1980 Fuel tonnage in the well is given separately of all fuel present in 1980.

1970-1980 (a) the engine pressure is given.

TABLE 100V
STEADY-STATE FLOW TIME MEASUREMENTS
MADE AT 26 CONCENTRATIONS OF THE POLYMER

Point	Applied Pressure			Total Solvent Fr. cm/sec.	Applied Viscosity cP/deg.	Temperature Solvent Fr. cm/sec.
	PSI/IN.	IN.	L.			
1	***	***	***	***	***	***
2	27.0	10.0	42.4	1075	700	650
3	28.0	41.0	44.0	1080	850	767
4	9.0	50.0	39.0*	1074	840	862
5	***	***	***	***	***	***
6	14.0	60.0	35.7	970	830	830
7	17.0	59.0	37.7	1000	750	850
8	20.0	47.0	30.11	1070	760	870

14.0 High Flow

Point	Applied Pressure			Total Solvent Fr. cm/sec.	Applied Viscosity cP/deg.	Temperature Solvent Fr. cm/sec.
	PSI/IN.	IN.	L.			
1	***	***	***	***	***	***
2	21.0	30.0	47.0	1044	1050	900
3	21.0	44.0	47.0	1044	1100	1100
4	9.0	50.0	40.0	1043	800	1080
5	***	***	***	***	***	***
6	10.0	61.0	36.0	1070	700	1000
7	16.0	53.0	38.0	1110	900	1000
8	18.0	49.0	32.7	1100	1070	1000

*From No. 1 via the slots in the wall in the direction of low flow pressure taps.

***Total flow inside the negative pressure region.

checking the assumptions listed in the "Statistical Assumptions" for the regression in a constant in Equation 2) that the pressure point in the center of the flow pattern points are not significantly in the flow field. Equation 2 does not have pressure point number 1 until presented with 50% of the data.

The velocity measurements at the other pressure points also took this form and all five axial distances showed approximately the same distributions. The pitch angle increased from the nose cone to the duct exit. The yaw angle and the radial angle decreased from the nose cone to the duct exit. At the inlet end up to eight diameter downstream, angles as high as 10 degrees were found near the nose cone of the flow field. The total velocity, axial velocity, and the tangential velocity all showed the same basic radial flow pattern. The velocities were uniform in the core, increased with radius and then slightly decreased into the wall. These patterns are similar to those found in the rotating flow presented with fluid cases (20).

In order to observe the changes in the flow as a function of axial distance from the inlet, the cross-sectional averages of the angle θ from 1966, and tangential velocity were calculated and presented in Figure 50 and plotted in Figures 14 and 15. All these parameters show a very distinct change in the behavior of tangential flow as was reported from the reported cases (20). The slopes have the same shape for both flow cases.

The high core flow for the measurements at 15 diameter downstream was confirmed by repeated measurements. These values may be due to a

TABLE 4.—
 AVERAGE CATCHES (G/T/1000) TAKEN
 ON A COMBINATION OF SHORTLY (SHORTLY) AND LONG (LONG)

Average Values For High Flow

Shortly Combination	4 Months	Average of Catch Area (g)	Temperature Average (°C/°F)	Long Combination
1	48 8	1.44 11.04	20.0	11.04
2	48 7	1.15 10.11	20.0	10.11
4	48 2	1.14 10.01	19.0	10.01
5	48 1	1.12 10.00	18.0	10.00
10	48 1	1.11 10.00	17.1	10.00

Average Values For Low Flow

Shortly Combination	4 Months	Average of Catch Area (g)	Temperature Average (°C/°F)	Long Combination
1	48 48	1.42 11.03	19.0	11.03
2	48 5	1.41 11.02	18.0	11.02
4	48 1	1.40 11.01	17.0	11.01
5	48 0	1.39 11.00	16.1	11.00
10	48 0	1.38 11.00	15.1	11.00

* Values of the Fall 11 11 11 11 11

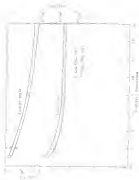


Figure 10. Average angle θ and the first two moments m_1 and m_2 as a function of λ .

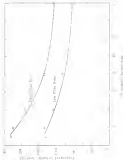


Figure 10 Decay of the longitudinal velocity component along the axis of the duct.

disturbance effect β_1 and not on the half of the first β_1 and β_2 distances of the swirling flow. The distance x_1 varies, depending on the intensity of disturbance, and the distance x_2 is connected to the fact that two of the streamlines cross within the vortex area. It can be seen from the vortex profiles that the vortex points had lower velocity values, and therefore the inclusion of the vortex points would lead to a higher velocity average.

Plotted in Figure 49 is the location of the vortex area with respect to the shear center. It can be seen that the swirling flow is indeed not symmetric and the location of the vortex area changes location with axial distance. Only one drawing is used to represent the difference for both high and low flow rates because the location for both conditions are almost identical.



Figure 48 Location of the negative feedback region in the complex plane

CHAPTER 1
SUMMARY OF THE EFFECTS OF PARTICLE SIZE
ON THE THERMAL FLUX DENSITY

A model has been developed and tested which describes particle transport phenomena as a function of particle characteristics, angle of illumination, and velocity vector. Together with the measurement of velocity components in a rotating flow it is possible to analyze the maximum rate errors that would occur when performing a limited analysis of the effluent stream following a cyclone.

For this simulation analysis, the volumetric flow rate and the particle sampling efficiency are calculated from velocity measurements obtained in the eight standard sampling locations using a 5-type probe rate (see Table XII and XIII). The angle of velocity vector, and particle velocity are determined from velocity measurements made at six cone locations using the four-hole probe rate (see Table XIII). The particle characteristics are obtained from particle size distribution data made by Brown [11] on knowledge the same system. From a particle distribution with a D₅₀ of 850 and geometric standard deviation of 2.00 (see Figure 11), the particle diameters were selected which represent the midpoint of 1% of the mass of the material (see Table XIV). The density of the particles was assumed to be 3.7 g/cm³. The major diameter was selected using the standard ellipse to be 0.001 m (1/8 inch). It is the author's not assumed that the ellipse would be aligned parallel with the axis of the stack and therefore, $\theta = 0$.

TABLE 1091
 1. YEAR AFTER YEAR MEASUREMENTS
 2. MEAN OF THE MEASUREMENTS FOR THE 100 YEAR PERIOD

Year	Annual Precipitation (mm. P_{100})	Mean Precipitation (mm. P_{100})	P_{100} (mm. P_{100})	P_{100} (mm. P_{100})	Precipitation (mm. P_{100})
1	0.00	-0.00	1.00	0.00	1000.0
2	0.00	0.00	1.00	0.00	1000.0
3	0.00	-0.00	1.00	0.00	1000.0
4	1.00	-0.00	0.00	0.00	000.0
5	-0.00	-0.00	-0.00	-0.00	000.0
6	0.00	-0.00	0.00	0.00	000.0
7	0.00	-0.00	0.00	0.00	000.0
8	0.00	-0.00	0.00	0.00	000.0
9	0.00	0.00	0.00	0.00	000.0

TABLE 1071
 5-DAY TEST TIME CHARACTERISTICS
 TYPICAL DATA FOR THE 5-DAY TEST METHOD

TEMP.	DOSSAGE CONCENTRATION mg/l	5-DAY PERCENTAGE CONCENTRATION	DO CONCENTRATION	DO CONCENTRATION	5-DAY PERCENTAGE CONCENTRATION
20	1.00	0.44	1.00	0.44	1700-4
17	1.00	-0.50	0.40	0.44	1000-1
14	1.00	-0.20	0.40	0.44	1000-1
11	1.00	-0.09	0.33	0.73	100-2
8	1.00	0.00	0.33	0.73	100-2
5	0.75	0.00	0.33	0.36	100-2
2	0.50	0.00	1.00	0.37	1000-1
1	0.25	0.10	1.00	0.30	1000-2

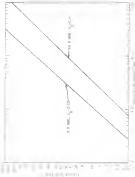


Figure 11: Graph showing the relationship between the number of nodes (N) and the number of edges (E) for a connected graph.

TABLE XVII
 REPORT PARTICLE SIZES
 FOR THE 18 PERCENT DISTILLATE OF No. 1
 CRACKED GASOLINE

Range	Distillate	Weight Percentage	Volume
0 - 10	0	0.04	0.00
10 - 20	10	1.01	0.00
20 - 30	20	1.70	0.00
30 - 40	30	1.58	0.00
40 - 50	41	1.70	0.00
50 - 60	50	2.15	0.00
60 - 70	60	3.00	0.00
70 - 80	71	4.00	0.00
80 - 90	80	4.00	0.00
90 - 100	90	10.40	0.00

Using these parameters, the average *inertial* (modified) Reynolds number Re with respect to pores was calculated as follows (Eq. (28))

$$A_p(A_p/d_p)(\bar{v}_p) = \frac{A_{p1}(\bar{v}_{p1}) + A_{p2}(\bar{v}_{p2}) + A_{p3}(\bar{v}_{p3})}{A_{p1} + A_{p2} + A_{p3}} \quad (28)$$

$$A_p(A_p/d_p)(\bar{v}_p) = \frac{A_{p1}(\bar{v}_{p1}) + A_{p2}(\bar{v}_{p2}) + A_{p3}(\bar{v}_{p3})}{A_{p1} + A_{p2} + A_{p3}} \quad (29)$$

$$A_p(A_p/d_p)(\bar{v}_p) = \frac{A_{p1}(\bar{v}_{p1}) + A_{p2}(\bar{v}_{p2}) + A_{p3}(\bar{v}_{p3})}{A_{p1} + A_{p2} + A_{p3}} \quad (30)$$

$$A_p(A_p/d_p)(\bar{v}_p) = \frac{A_{p1}(\bar{v}_{p1}) + A_{p2}(\bar{v}_{p2}) + A_{p3}(\bar{v}_{p3})}{A_{p1} + A_{p2} + A_{p3}} \quad (31)$$

$$A_p(A_p/d_p)(\bar{v}_p) = \frac{A_{p1}(\bar{v}_{p1}) + A_{p2}(\bar{v}_{p2}) + A_{p3}(\bar{v}_{p3})}{A_{p1} + A_{p2} + A_{p3}} \quad (32)$$

$$A_p(A_p/d_p)(\bar{v}_p) = \frac{A_{p1}(\bar{v}_{p1}) + A_{p2}(\bar{v}_{p2}) + A_{p3}(\bar{v}_{p3})}{A_{p1} + A_{p2} + A_{p3}} \quad (33)$$

where A_p = total aperture coefficients for porous plate p

\bar{v}_p = total velocity at sampling velocity at p

θ = angle of flow at point p relative to the axis of the duct

\bar{v}_{p1} = total velocity based on the particle diameter (total velocity)

at p_1 and particle diameter d_{p1}

d_{p1} = smallest particle diameter and representing 1% of the total mass

Since the sampling velocity will decrease the value of air sampled at each pressure point, the total apertures coefficient for each flow rate was interpreted by taking an average weighted velocity as sampling velocity:

$$A_p = \frac{A_{p1}(\bar{v}_{p1}) + A_{p2}(\bar{v}_{p2}) + A_{p3}(\bar{v}_{p3}) + A_{p4}(\bar{v}_{p4}) + A_{p5}(\bar{v}_{p5})}{\bar{v}_{p1} + \bar{v}_{p2} + \bar{v}_{p3} + \bar{v}_{p4} + \bar{v}_{p5}} \quad (34)$$

where \bar{v}_{p1} = total velocity at pressure point p

Results of the mixing tank at point 1 and impeller pressure curves at point 2 above the pressure points were not used in the analysis.

The total experimental uncertainties amounted to ± 0.1 percent. The low and high flow measurements are ± 0.02 percent (Table III and III). Thus, regarding the experimental limits of measurement error found in this analysis, the reason is that the low velocities during sampling were, on the average, not significantly smaller than the high velocities in the opposite direction. The large error value detected is probably less than or equal to the actual velocity which could lead to subnormal sampling, producing an increased uncertainty. The small misalignment when sampling parallel to the main wall could produce a decreased uncertainty. To rule out these errors has a tendency of reducing the error margin.

Similar reasons for the small errors are the small size of the account. The figures indicate the over 90% of the particles were less than 0.2 and 0.1 for the low and high flow rates respectively. These values lead to small sampling errors, even when subnormal sampling conditions are not maintained.

From experimentally determined that the millimeter efficiency should be on the order of 60-70%. Since the flow rate used by Hagen was approximately midway between the high and low flow rates in this study, the flow profiles should be approximately the same. The discrepancy between Hagen's experimental values and the values predicted by the discussion probably can be accounted for by experimental error by Hagen. It could be easily responsible to obtain a 60% sampling error for an assumed, as well as the one used without extreme valuations, sampling conditions. Hagen also found a 40% error when sampling at the angle indicated with

TABLE VIII
 IRRADIATION PROPERTIES
 FOR POLYMER 15, THE IRRADIATION BEAM, FOR THE LOW TEMPERATURE

Point	Amplitude Relative From p-Tyrosine Total Yield (Relative)	From Voluntary Dose - Beta Phase Yield (Relative)	β Decay	β Phase	Relative Yield
1	1000	***	1.40	1.00	1.00
2	1000	1000	1.40	1.00	1.00
3	1000	1000	1.40	1.00	1.00
4	1000	1000	1.40	1.00	1.00
5	1000	1000	1.40	1.00	1.00
6	1000	1000	1.40	1.00	1.00
7	1000	1000	1.40	1.00	1.00
8	1000	1000	1.40	1.00	1.00
9	1000	1000	1.40	1.00	1.00
10	1000	1000	1.40	1.00	1.00

Relative Average = 1.00

TABLE 301
ADAPTATION COEFFICIENTS
(continued) 3. THE ADAPTATION MODEL FOR THE 1980-2020 PERIOD

Scenario	Deep/Long Tailwater Base 3 Type Factor Value (continued)	Base Location Base 3 Relocation Value (continued)	1 Coefficient	2	3 (Base)
1	1070.0	1000	1.14	1.00	1.00
2	1090.7	1000	1.00	1.00	1.00
3	1080.0	1000	1.00	1.00	1.00
4	1000	1000	1.00	1.00	1.00
5	780.0	1000	1.00	1.00	1.00
6	1070.7	1000	1.00	1.00	1.00
7	1070.7	1000	1.00	1.00	1.00
8	1070.0	1000	1.00	1.00	1.00
Weighted Average					1.00

The authors do. From Figure 11, \bar{r} is assumed equal to averaging the differences between the angles where two adjacent boundary points are equally. It should be possible to partition the perimeter of the sample into equal angles. This means that the sample reliability increases as the 5-type pitot tube will be approximately the same as the true total velocity and therefore, the sampling error should be no greater than the range of 70 degrees or 0.21. This could represent the maximum error for a 1000 ft/sec stream and would be much less for the stream used in the study. Since Davis's sampling error is clearly less than as high as the theoretical maximum, it must be expected to give flow as the experimental value.

It seems to me how much greater the error would be for larger velocities. A similar analysis was performed using a distribution and a 10 ft/sec with diameter and 2.5 geometric standard deviation (see Figure 10). This was the distribution obtained at the outlet of a turbine in a hot air engine plant (20). Because of the longer diameter provided the sampling efficiency was reduced to 0.700 for the high flow condition.

The velocity flow rates determined from the 5-type pitot tube measurements are compared with the flow rates calculated from Pitot-static probe tube measurements in Table 10. The total flow rates using the five hole pitot tube data were included in multiplying the average velocity by the total duct area minus the core area. The flow rates using the 5-type pitot tube data were determined using two different methods varying in how the velocity indicator at port four is located

1993, 2003

Is there a net energy input or output with
the water treatment?

Period (year)	Flow	Concentration	Flow Rate ³	Flow Rate ³	Process Unit ¹	Relative value ²
Input	Output	Input/Flow	Output/Flow	Input/Flow	Output/Flow	Input/Flow
1993-2003	1.00	0.002	1.00	1.00	1.00	1.00
1993-2003	0.98	0.004	1.00	1.00	1.00	1.00
1993-2003	0.98	0.004	1.00	1.00	1.00	1.00

1. Negative value is indicated in the column of process unit.

2. Negative value is shown in the column of energy input.

In the first method, the negative magnitude was limited to 0.17544 the average axial velocity. The calculated flow rate was obtained by multiplying the average axial velocity by the flow area (sectional area). In the second method, the negative value is used as the absolute value of the average velocity and the section under flow area is used to determine the flow rate.

The results presented in Table IV, show that the inaccuracy of the 2-type plate tube to two angle produces a higher calculated flow rate by approximately 40%. By incorporating the negative value in the average velocity determination, this error is reduced to 17%.

It should be noted that the 2-type plate tube does not vary well. This could be explained from looking at the characteristics of the plate tube to two angle (Figure 14). When the incidence angle had a two angle (i.e.) that approximately 18 degrees, the 2-type plate tube readings were 10% close to the total velocity. However, beyond angles of 18 degrees, the plate tube readings drop off quite rapidly and at 75 degrees, the plate tube was reading a value of 44% that one fifth of the true value.

The errors for both sampling efficiency and flow rate determination are presented in Table III for the three simulated conditions. The sampling errors and flow rate errors are in opposite directions so that when the Po values are combined to determine velocity error, the overall effect is reduced.

CHAPTER VI SUMMARY AND RECOMMENDATIONS

6. Summary

Results of experiments in this study have led to a better understanding of the types and magnitude of errors that are involved when attempting to obtain a representative sample of particulate matter from gas stream with complex flow patterns. The errors induced by turbulent flow were analyzed from two separate approaches. The first involved analysis of particle size plug errors as a function of particle deceleration, sampling velocity relative to the flow stream velocity, and angle of the nozzle relative to the direction of flow. The second involved analysis of swirling flow patterns and their subsequent effects on flow measurements made by the 5 type pitot tube.

Particle sampling errors as a function of velocity ratios and angle of nozzle/plug were studied by taking asymptotic maximum and minimum samples from a straight section of duct. By analyzing the problem in this fashion the flow situations are more readily and more easily seen applications beyond this study. They provide developmental information for a better understanding of the inertial effects in aerosol sampling.

The flow measurement errors were analyzed by sampling the static flow pressure in the wall of a cyclone using a flush-hole probe tube. Cross and axial profiles were measured at three radial distances along the duct to determine how the flow profile changes as it moves up the duct. 5 type pitot tube measurements were taken and compared to the results of the flush-hole probe tube measurements.

The aim of one of the study, individual sampling along the flow measurement was satisfied in a simulation using an appropriate magnitude of errors due to the method of measuring rate is determined on the basis of a system.

A summary of the important results investigated flow characteristics are follows:

A. The flow pattern found in a tank following the exit of a small industrial system are of such a nature that in order to estimate reliably or obtain a representative sample with the process not being under equipment angles is taken at 75 degrees relative to the tank that are found in some parts of the flow. Some large scale industrial tank in working flow is absolutely well preserving its fluid state, it decays very slowly as it moves up the tank and therefore sampling at any random direction of the system will involve the same problem.

B. The gas characteristics of the bridge pipe make hard to control types of errors that lead to a horizontal flow stream. When the angle of gas is less than 45 degrees the measured velocity is greater than or equal to the actual velocity with the maximum error being approximately 20% beyond 45 degrees the measured velocity drops off quite rapidly and at an angle of 75 degrees the measured velocity is less than half the true velocity. Because of this gas characteristics the bridge pipe rate is not suitable for decomposing the axial component of flow from the total flow which includes the tangential component. Subsequent flow calculations based on bridge pipe rate measurements in a working flow were found to be in excess of the actual flow by as much as 50%.

C. Final tubes based on the β -ray range and momentum analysis. It would thus be desirable to determine the relative contribution of a magnetized flow field. The final tube just has the advantage of giving pitch information as well as the β -ray angle. However, in a typical flow system, the β -ray angle is of much greater magnitude than the pitch angle and therefore, the pitch angle can be ignored with small error. In the situation studied, if pitch angle were ignored, the calculated flow rate would be in error by less than 5%.

D. The particle coupling errors due to misalignment coupling velocity and nuclei misalignment were analyzed and a model was developed to describe the coupling efficiency as a function of velocity ratio (V_0), misalignment angle (θ_0), particle diameter (particle velocity), and nuclei diameter. It was found that the nucleus error for $k = 1$, approached $(1 - \cos \theta_0)$. When both a nuclei misalignment and misalignment coupling velocities are involved then the nucleus error approaches $(1 - \cos \theta_0)^2$. The equations and their limiting conditions for predicting the separation coefficient are summarized in Table 1001.

E. The Fisher number adequately describes the general characteristics of particle coupling. However, when the nuclei is aligned to the flow stream there is no apparent change in the general properties which is due to a reduced projected nuclei diameter. A correction factor was developed to adjust the Fisher number to take this into account.

F. When the probe wall was analyzed separately from the balance, it was found that as much as 50% of the probe particulates become entrained

1. The first part of the problem is to find the value of α such that the function $f(x) = \alpha x^2 + (1-\alpha)x + 1$ is a probability density function. This means that $f(x) \geq 0$ for all x and $\int_{-\infty}^{\infty} f(x) dx = 1$.

Solution:

$$\begin{aligned}
 \int_{-\infty}^{\infty} f(x) dx &= \int_{-\infty}^{\infty} (\alpha x^2 + (1-\alpha)x + 1) dx \\
 &= \alpha \int_{-\infty}^{\infty} x^2 dx + (1-\alpha) \int_{-\infty}^{\infty} x dx + \int_{-\infty}^{\infty} 1 dx \\
 &= \alpha \left[\frac{x^3}{3} \right]_{-\infty}^{\infty} + (1-\alpha) \left[\frac{x^2}{2} \right]_{-\infty}^{\infty} + \left[x \right]_{-\infty}^{\infty} \\
 &= \alpha \left(\frac{\infty^3}{3} - \frac{(-\infty)^3}{3} \right) + (1-\alpha) \left(\frac{\infty^2}{2} - \frac{(-\infty)^2}{2} \right) + (\infty - (-\infty)) \\
 &= \alpha \left(\frac{\infty^3}{3} + \frac{\infty^3}{3} \right) + (1-\alpha) \left(\frac{\infty^2}{2} - \frac{\infty^2}{2} \right) + \infty \\
 &= \alpha \left(\frac{2\infty^3}{3} \right) + 0 + \infty \\
 &= \frac{2\alpha}{3} \infty^3 + \infty
 \end{aligned}$$

$$\begin{aligned}
 \frac{2\alpha}{3} \infty^3 + \infty &= 1 \\
 \frac{2\alpha}{3} \infty^3 &= 1 - \infty \\
 \frac{2\alpha}{3} &= \frac{1 - \infty}{\infty^3} \\
 \frac{2\alpha}{3} &= 0 \\
 \alpha &= 0
 \end{aligned}$$

the article was collected on the $\text{max}(j)$ basis. This has the effect of not only on the importance of using the $\text{max}(j)$ basis in the final analysis but more importantly it implies that there are no practical problems in choosing various particles as a function of j values such as an integer. If the collection of particles in the article as particles were dependent, then errors in the code could lead to particle mixing errors.

4. A random walk model was developed which incorporates the information obtained in this study on particle sampling errors and on the mixing time. The particle sampling efficiency is a function of the stream size as expected a function of particle size for a particle distribution with a mean mass diameter (PMD) of 1.0 μm and a geometric standard deviation of 2.0. The sampling errors predicted were less than 10%. For a larger distribution with a mean mass diameter of 10.0 μm and geometric standard deviation of 2.0, a 10% sampling error was predicted. One of the reasons that the sampling errors were as small as these were is that the two sections including sampling from product streams in opposite directions. The assignment of the results shown by the temporal velocity component leads to a reduction of single measurement. The reduced sampling variance exhibited from 1 type point take measurements leads to substantially sampling not an increased single measurement. When these two sections are combined, the total error is reduced somewhat depending upon the magnitude of the two errors.

3.2. Instrumentation

It is commonly stated that if the average angle of the flow is between 7.5° and 11° off the vertical, it is greater than 10° degrees. This (21) measure should not be performed. Since the maximum error in particle counting has been found to be 4.1 ± 0.0005 , the 10° degree measurement (± 0.0005) resolution and $\pm 10^\circ$ degree limitation could be more appropriate. For a 10° degree angle, the velocity measured by the B-type pilot tube would be approximately the same as the true velocity ($C_D = 1$, $k = 1$). Therefore, the maximum error would be $11 \pm \sin(10^\circ)$ or 15 for a very large animal.

When studying flow that will move in a single, well predictable water environment, the flow of water in another location because of the physical interaction of these organisms, a better approach would be to utilize Method 2 as this it could be used as a compensated flow sensor. By replacing the B-type pilot tube with a thermocouple pilot tube, the direction of the flow could be accurately determined for clipping the turtle, and the velocity component could be measured for a correct calculation of volumetric flow rate. In addition to the B-type hole pilot tube, the instrument could have to include a pressure transducer to measure the flow angle, an extra thermocouple and a method of rotating the probe without rotating the turtle (perhaps two

REFERENCES

1. Standards of Performance for Soil Measurement Methods. International Union of Pure and Applied Chemistry, 1971.
2. Bureau of Reclamation Method 3-4. Federal Register, 17(1982) 41595, 1982.
3. Riley, J. R. Sampling Size and Sampling of Surface Fertilizers. Analytical Determination of Soil. McGraw-Hill, New York, 1977, p. 5.
4. Gaudin, R. P. and G. G. Shepherd. Calculation of Fertilizer Trajectories. Soil Res. Chem., 1977, 401-404.
5. Gaudin, R. P. Effect of Soil on Accurate Sampling of Aqueous. Soil Res. Chem. 1977, 71-75.
6. Gaudin, R. P., R. P. Gaudin, G. P. Anderson and L. J. Brown. Analytical. Analytical Methods. Soil Res. Chem., 1977, 108-110.
7. Gaudin, R. P. and G. P. Anderson, Jr. The Importance of Control in Soil Res. Sampling. Adv. Agron., 1977, 102-104.
8. Gaudin, R. P. and L. J. Brown. The Effect of Fertilizer Shape on the Accuracy of Sampling. The Effect of Fertilizer Shape on the Accuracy of Sampling. J. Soil Res., 1977, 102-104.
9. Gaudin, R. P. and L. J. Brown. Sampling with a Soil Res. Plate. Soil Res. Chem. 1977, 102-104.
10. Gaudin, R. P. Collection of Soil Res. Data. Fertilizer by Means of an Analytical Sampling Probe. Soil Res. Chem. 1977, 102-104.
11. Gaudin, R. P. The Importance of Control. The Analytical Chem. New York, 1977, p. 70.
12. Gaudin, R. P. and L. J. Brown. Investigation of Aqueous Sampling by Photographing Fertilizer Under Micro Film Illustration. J. Soil Res., 1977, 102-104.
13. Gaudin, R. P. and L. J. Brown. Techniques for Collection of Aqueous. Soil Res. Chem. 1977, 102-104.

10. Berman, E. H. Sampling of Solids and Suspensions. *Analyst*, 1971, 96, 1, 1071-1075.
11. Berman, E. H. Sampling of Submicronmic Particles Suspended in Gas. *Recent and Upcoming Four Days of Air*. Presented at the second Meeting of the Air Pollution Control Association, Toronto, Canada, 1977.
12. Schulz, G. Particle Sampling Bias Induced by Jetted/Gas Jet Sampling and Deposition within the Sampling Line. *Aerosol Sci. Technol.* 1979, 2(2), 73-83.
13. Christiansen, W. The Geometrical Dependence of Air Sampling. *Aerosol Sci. Technol.* 1979, 2(2), 133-140.
14. Sherell, D. E. Variation in Relative Efficiency of a Filter Sampler with Gas Speed, Flow Rate Angle and Particle Size. *Aerosol Sci. Technol.* 1979, 2(2), 284-292.
15. Tschun, V. A. Sampling of Solids. *Aerosol Sci.*, 8, 287-293.
16. Lallier, A. G. Application of an Aerosol Jet to Ventilate Tube from a Filter Treatment to a) HEPA-HEPA Foreign Technology Barriers. *Graphical Illustration Air Force Tech. Rep.* 1972.
17. Sherell, D. E. Theoretical Limits of Error Due to Jetted/Gas Jet Sampling of Particulate Matter. *J. Air Pollut. Control Assoc.* 1973, 23, 1250.
18. Sherell, D. E. Sampling of the Sampling Probe in Turbulent Flow. M. S. Thesis, University of Toronto, Canada, 1974.
19. Baker, D. W. and C. L. Soper. Some of Sampling Techniques Flow of Aerosolizable Fluids in Long Pipes. *Flow, Its Measurement and Control in Science and Industry, Volume 1, Part 1, Flow Characterization*. Institution Society of America, Pittsburgh, 1975, p. 301.
20. Dugger, W. A. Velocity Measurement in Water Pipes. *Flow, Its Measurement and Control in Science and Industry, Volume 1, Part 1, Flow Characterization*. Institution Society of America, Pittsburgh, 1975, p. 285.
21. Sherell, D. E. and D. P. Sherell. Effective Sampling Techniques for Particulate Matter from Diffuse Particulate Sources. EPA-600/3-77-030. U.S. Environmental Protection Agency, Research Triangle Park, N.C., 1977.
22. Berman, E. H. and E. L. Williams. Pressure Drop and Flow Measurement and the Sampling of Aerosols. *Flow Measurement and Control in Science and Industry, Volume 1, Part 1, Flow Characterization*. Institution Society of America, Pittsburgh, 1975.

10. Ayres, R. P. and J. A. Smith. "Pilot Field Experiments for the Identification and Measurement of Flow." *Water Sampling News*, November, 1973.
11. Brown, R. A., J. J. Gerhart, J. E. Morgan and J. A. Turner. "Particulate Sampling Strategies for Large River Flows: Testing the Southern Flow Study's Results." U. S. Environmental Protection Agency, Research Triangle Park, N. C., 1979. 247 pp.
12. Higgins, F. J. and J. E. Schaeffer. "A Study on the Accuracy of Type B Flow Rate." EPA 600/3-79-006. U. S. Environmental Protection Agency, Research Triangle Park, N. C., 1979.
13. Lee, J. P. and R. J. Pryor. "Flow Velocity Measurements on Solpiling Flow on a Pipe Flow Test Apparatus and Issues in Design and Industry." Volume 1, Part 1. Flow Characterization. International Society of Marine Engineers, Pittsburgh, 1973, p. 181.
14. Green, R. L. and R. L. Lane. "Particulate Loads." *Water, Sediment and Stone*. E. F. O. Ayres, Ed. London, 1987, p. 81.
15. "The Pollutants Manual." Item 56. General Parameters. *Water and Wye Journal*, Bristol, 1988, p. 4.
16. Mulvey, R. P., G. A. Langston and C. H. Pearson. "Nonpoint-source Landfill Construction." *J. Air and Waste Poll.*, 1978, 10:11.
17. Perry, J. E. "Chemical Engineers' Handbook," McGraw-Hill New York, 1981.
18. "Fluvial Transport Handbook." *Water and Wye Journal*, New York, 1988.
19. "Wind Effects: Their Theory and Applications." R. L. Jeon, Ed. *Water and Wye Journal*, New York, 1978.
20. "Statistics, F. G. Measurement Systems, Applications and Design." McGraw-Hill, New York, 1978.
21. DeCh, P. R. "The Effects of Sample Design and Sampling Techniques on Polluted Measurements." EPA 600/3-79-005. U. S. Environmental Protection Agency, Washington D. C., 1979. 89 pp.
22. "Manual of Procedures for Chemical Procedures." G. L. Tatum, Executive. *Water and Wye Journal*, 1973.
23. "Sampling Techniques of Physics Handbook." P. J. Gray, Ed. McGraw-Hill New York, 1977.

41. Gilman, J. A. The Reactivity of Immune Particles Produced in a Splitting Virus Antigen System. *Acad. Sci. New York*, 1961, 261, 1961
42. George Langley Marshall. Control Program Management Division, Air National Training Institute, Research Triangle Park, N. C., 1955
43. Gaudin, J. A. *AFM Polymers Engineering Manual*, (In preparation) Production Agency, 1957b, AFM, Research Triangle Park, N. C., 1957

BIOGRAPHICAL SKETCH

WILLIAM J. HARRISON born at Hazleton, Pa., 1886, the son of Mrs. J. W. Harrison, a member of the Quaker family. Received, 1908, B.S. in Civil and Mechanical Engineering from the University of Pennsylvania, and two high schools in Hazleton, Pa. and Berkeley, California and Berkeley. He studied two years at Brown with German and Latin and at the Pennsylvania State University, where he received a B.S. in American Engineering in 1911. His next three years were spent working with the Electrical Division of General and the American Field-Coulter Association at Washington, D.C. In September 1914 he began his graduate education in Environmental Engineering Sciences at the University of Florida. After receiving a Master of Engineering in March, 1917, he stayed on at the university as a graduate research assistant, as part of a Ph.D. For three years, the results of which is a book on "The Florida River".

I certify that I have read this study and that in my opinion it conforms to acceptable standards of scholarly presentation and is fully adequate, in scope and quality, as a dissertation for the degree of Doctor of Philosophy.


John L. Kunkin, Chairman
Professor of Environmental
Engineering Sciences

I certify that I have read this study and that in my opinion it conforms to acceptable standards of scholarly presentation and is fully adequate, in scope and quality, as a dissertation for the degree of Doctor of Philosophy.


Paul H. Hines
Professor of Environmental
Engineering Sciences

I certify that I have read this study and that in my opinion it conforms to acceptable standards of scholarly presentation and is fully adequate, in scope and quality, as a dissertation for the degree of Doctor of Philosophy.


Robert C. Huber
Professor of Environmental
Engineering Sciences

I certify that I have read this study and that in my opinion it conforms to acceptable standards of scholarly presentation and is fully adequate, in scope and quality, as a dissertation for the degree of Doctor of Philosophy.


William C. Hines
Professor Emeritus of
Physics and Nuclear Engi-
neering Sciences

This dissertation is deposited in the Graduate Library of the University of Chicago at Engineering 31, 55, Eastern Division, and is accepted in partial fulfillment of the requirements for the degree of Doctor of Philosophy.

August, 1979

Robert G. Barr

From College of Engineering

From Graduate Library